Energy Storage Materials 52 (2022) 371–385

Contents lists available at ScienceDirect

Energy Storage Materials

journal homepage: www.elsevier.com/locate/ensm

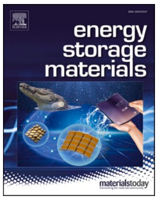

Effect of particle size on thermodynamics and lithium ion transport in electrodes made of $Ti_2Nb_2O_9$ microparticles or nanoparticles

Yucheng Zhou [a], Etienne Le Calvez [b,c], Sun Woong Baek [a], Matevž Frajnkovič [a], Camille Douard [b,c], Eric Gautron [b], Olivier Crosnier [b,c], Thierry Brousse [b,c], Laurent Pilon [*,a,d,e]

[a] Mechanical and Aerospace Engineering Department, Henry Samueli School of Engineering and Applied Science, University of California, Los Angeles, CA 90095, USA
[b] Nantes Université, CNRS, Institut des Matériaux de Nantes Jean Rouxel, IMN, 44000 Nantes, France
[c] Réseau sur le Stockage Électrochimique de l'Énergie (RS2E), CNRS FR 3459, 33 rue Saint Leu, 80039 Amiens, France
[d] California NanoSystems Institute, University of California, Los Angeles, CA 90095, USA
[e] Institute of the Environment and Sustainability, University of California, Los Angeles, CA 90095, USA

ARTICLE INFO

Keywords:
Lithium-ion battery
Entropic potential
Intercalation
Galvanostatic intermittent titration technique
Calorimetry
Thermal management

ABSTRACT

This study compares the charging mechanisms, thermodynamics, lithium ion transport, and *operando* isothermal calorimetry in lithium-ion battery electrodes made of $Ti_2Nb_2O_9$ microparticles or nanoparticles synthesized by solid-state or sol-gel methods, respectively. First, electrochemical testing showed that electrodes made of $Ti_2Nb_2O_9$ nanoparticles exhibited larger specific capacity, smaller polarization, and better capacity retention at large currents than those made of $Ti_2Nb_2O_9$ microparticles. Furthermore, potentiometric entropy measurements revealed that electrodes made of either $Ti_2Nb_2O_9$ microparticles or nanoparticles showed similar thermodynamics behavior governed by lithium intercalation in solid solution, as confirmed by *in situ* XRD measurements. However, electrodes made of $Ti_2Nb_2O_9$ nanoparticles featured smaller overpotential and faster lithium ion transport than those made of $Ti_2Nb_2O_9$ microparticles. In fact, *operando* isothermal calorimetry revealed smaller instantaneous and time-averaged irreversible heat generation rates at electrodes made of $Ti_2Nb_2O_9$ nanoparticles, highlighting their smaller resistive losses and larger electrical conductivity. Finally, the measured total heat generation over a charging/discharging cycle matched the measured net electrical energy loss. Overall, $Ti_2Nb_2O_9$ nanoparticles synthesized by the novel sol-gel method displayed excellent cycling performance and reduced heat generation as a fast-charging lithium-ion battery anode material. These features present major advantages for actual battery systems including larger energy and power densities, simpler thermal management, and enhanced safety.

1. Introduction

Fast-charging lithium-ion batteries (LIBs) constitute a promising technology amid the global transition towards renewable energy and widespread electrification. The anode material of fast-charging commercial LIBs is generally graphite. However, graphite inserts lithium ions at potential close to 0.1 V vs. Li/Li^+. This can result in the formation of solid electrolyte interphase (SEI) and dendrites and eventually overheating and short circuiting of the battery [1,2]. Moreover, the limited lithium ion mobility in graphite reduces the specific capacity during fast charging. To address these issues, alternative anode materials have been proposed to enable fast charging at potentials above 1.0 V vs. Li/Li^+. Among those, transition metal oxides such as $Li_4Ti_5O_{12}$ [3,4], Nb_2O_5 [5,6], and $TiNb_2O_7$ [7] have emerged as anode materials of choice. In addition, Wadsley-Roth shear phase materials such as $Nb_{18}W_{16}O_{93}$ [8] and PNb_9O_{25} [9] have shown impressive rate capabilities. This has prompted great interest in understanding the mechanisms behind such performance. For example, a recent series of studies on PNb_9O_{25} [9–11] used multiple characterization techniques to gain insight into the electrochemical processes, structural and property changes occurring in the material during cycling. These studies found that the corner-sharing and edge-sharing NbO_6 octahedra not only facilitated the fast diffusion of lithium ions in the structure, but also permitted relatively small change of the cell volume during cycling.

$Ti_2Nb_2O_9$ is another promising transition metal oxide offering large specific capacity and small cycling degradation [12]. The topotactic

---

* Corresponding author.
E-mail address: pilon@seas.ucla.edu (L. Pilon).

https://doi.org/10.1016/j.ensm.2022.08.010
Received 22 May 2022; Received in revised form 8 July 2022; Accepted 4 August 2022

dehydration of the lamellar-structured $HTiNbO_5$ gives rise to the tunnel-structured $Ti_2Nb_2O_9$. The tunnels are formed by 2 × 2 units of edge-sharing octahedra connecting their corners along the a- and c-axes. Moreover, the crystallographic structure of $Ti_2Nb_2O_9$ is close to a Wadsley-Roth structure due to its units of edge-sharing octahedra. Therefore, $Ti_2Nb_2O_9$ should also exhibit excellent cycling performance, especially during fast charging. However, Colin et al. [13] first reported a reversible specific capacity for $Ti_2Nb_2O_9$ electrodes in 1 M $LiPF_6$ in EC:DMC 1:1 w/w electrolyte of only 144 mAh/g at C/10 compared with the theoretical specific capacity of 252 mAh/g. A more recent study [14] performed ion exchange from $KTiNbO_5$ to $HTiNbO_5$ to NH_4TiNbO_5 followed by thermal decomposition of NH_4TiNbO_5 to synthesize $Ti_2Nb_2O_9$ microparticles. The corresponding electrodes achieved a reversible specific capacity of 201 mAh/g at C/10 in 1 M $LiPF_6$ in EC:DMC 1:1 v/v electrolyte. Nevertheless, the $Ti_2Nb_2O_9$ in both studies did not present sufficient capacity retention at large currents for potential applications as a fast-charging LIB anode material.

Here, we hypothesize that one way to approach the theoretical specific capacity of $Ti_2Nb_2O_9$ is to decrease the particle size to nanoscale and increase the nanoporosity to facilitate access and transport of lithium ions. First, electrodes with smaller particles generally have larger electrical conductivity which is crucial in reducing resistive losses during cycling [15,16]. Moreover, decreasing the particle size of an electrode material generally leads to better capacity retention at high C-rates [17]. This can be explained by considering the diffusion length L given by Fick's first law of diffusion as $L\propto\sqrt{Dt}$ where D is the lithium ion diffusion coefficient and t is the diffusion time. Decreasing the particle size shortens the time required for lithium ion insertion into the host material, thereby enabling faster charging and discharging [17]. Finally, in some cases, even the same material composition can feature very different charging mechanisms and/or thermodynamics behavior depending on the particle size [18]. For example, during delithiation of Li_xFePO_4, a lithium-rich and a lithium-poor phase could coexist in the 170-nm nanoparticles but not in the 40-nm nanoparticles [19]. In addition, during lithiation of anatase TiO_2, the 130-nm nanoparticles featured different two-phase coexistence regions in the open-circuit voltage compared to the 15-nm nanoparticles [20]. Several studies [21–23] investigated nanosheets of $Ti_2Nb_2O_9$ as a sodium-ion battery electrode material. The nanosheets were produced after an exfoliation process of the bulk material. However, they showed poor stability as the restacking of exfoliated nanosheets led to an abrupt and irreversible formation of agglomerate microparticles. Therefore, more stable nanostructures are desirable in particular for use in lithium-ion batteries considering their superior gravimetric and volumetric energy densities compared to sodium-ion batteries. In fact, to the best of our knowledge, the synthesis and characterization of more stable $Ti_2Nb_2O_9$ nanoparticles as a lithium-ion battery electrode material has not been reported to date. Note that several studies [24–26] have provided in depth reviews of the general benefits and drawbacks of nanomaterials for electrical energy storage.

This study presents a novel sol-gel method to synthesize mesoporous $Ti_2Nb_2O_9$ nanoparticles [27]. The structures and performance of electrodes made of $Ti_2Nb_2O_9$ nanoparticles were systematically compared with those made of $Ti_2Nb_2O_9$ microparticles synthesized by the traditional solid-state method [13]. Characterization techniques including *in situ* X-ray diffraction (XRD), cyclic voltammetry, and galvanostatic cycling were combined with state-of-the-art potentiometric entropy measurements and *operando* isothermal calorimetry. Together they should reveal the effect of the particle size on the electrochemical cycling performance, thermodynamics behavior, and lithium ion transport in $Ti_2Nb_2O_9$ electrodes. Overall, this study aims to extend our general understanding of transition metal oxides as fast-charging LIB electrode materials by optimizing their particle size to achieve better performance and cycling stability and to reduce electrical losses and heat generation.

2. Background

2.1. Potentiometric entropy measurements

Potentiometric entropy measurements consist of determining the open-circuit voltage $U_{OCV}(x,T)$ and entropic potential $\partial U_{OCV}(x,T)/\partial T$ of a battery cell at constant temperature T and pressure as functions of lithium composition x, specific capacity C_m, or state of charge. Our previous study [11] has not only described the fundamental relationships between $U_{OCV}(x,T)$, $\partial U_{OCV}(x,T)/\partial T$, and the material thermodynamics properties, but also proposed an interpretation guide of their measurements. In brief, the open-circuit voltage $U_{OCV}(x,T)$ of a battery cell with a $Ti_2Nb_2O_9$ working electrode and a lithium metal counter electrode can be expressed as [11,28],

$$U_{OCV}(x,T) = -\frac{1}{e}\left[\frac{\partial g_{TNO}(x,T)}{\partial x} - g^{\circ}_{Li}(T)\right] \tag{1}$$

where e is the elementary charge, $g_{TNO}(x,T)$ is the Gibbs free energy of $Li_xTi_2Nb_2O_9$ per unit of $Ti_2Nb_2O_9$, and $g^{\circ}_{Li}(T)$ is the standard Gibbs free energy per unit of lithium metal independent of x. Similarly, the entropic potential $\partial U_{OCV}(x,T)/\partial T$ can be expressed as [11,29],

$$\frac{\partial U_{OCV}(x,T)}{\partial T} = \frac{1}{e}\left[\frac{\partial s_{TNO}(x,T)}{\partial x} - s^{\circ}_{Li}(T)\right] \tag{2}$$

where $s_{TNO}(x,T)$ is the entropy of $Li_xTi_2Nb_2O_9$ per unit of $Ti_2Nb_2O_9$ and $s^{\circ}_{Li}(T)$ is the standard entropy per unit of lithium metal also independent of x. The evolution of $U_{OCV}(x,T)$ and $\partial U_{OCV}(x,T)/\partial T$ during lithiation and delithiation can give insight into the charging mechanisms of the battery cell including lithium ion insertion in a homogeneous solid solution, two-phase coexistence, phase transition, and intralayer lithium ion ordering [11,30].

Moreover, the apparent diffusion coefficient $D_{Li^+}(x,T)$ of lithium ions in the $Ti_2Nb_2O_9$ working electrode can be estimated from galvanostatic intermittent titration technique (GITT) measurements based on Fick's second law of diffusion according to [31],

$$D_{Li^+}(x,T) = \frac{4}{\pi\tau}\left(\frac{V_{TNO}}{A_{TNO}}\right)^2\left[\frac{\Delta U_{OCV}(x,T)}{\Delta V(x,T)}\right]^2. \tag{3}$$

Here, τ is the duration of the current pulse, A_{TNO} and V_{TNO} are respectively the surface area and volume of the $Ti_2Nb_2O_9$ working electrode, $\Delta V(x,T)$ is the cell potential change caused by the current pulse but excluding the initial IR drop, and $\Delta U_{OCV}(x,T)$ is the open-circuit voltage change caused by the current pulse.

2.2. Heat generation in batteries

The instantaneous total heat generation rate $\dot{Q}_T(x,T)$ (in W) in a battery cell can be divided into several contributions including (i) Joule heating $\dot{Q}_J(x,T)$, (ii) reversible entropic heat generation $\dot{Q}_{rev}(x,T)$, (iii) enthalpy or heat of mixing $\dot{Q}_{mix}(x,T)$, and (iv) heat generation due to side reactions $\dot{Q}_{sr}(x,T)$, i.e. [11,30,32–34],

$$\dot{Q}_T(x,T) = \dot{Q}_J(x,T) + \dot{Q}_{rev}(x,T) + \dot{Q}_{mix}(x,T) + \dot{Q}_{sr}(x,T). \tag{4}$$

The heat generation rate $\dot{Q}_i(x,T)$ is positive (or negative) when the associated phenomena are exothermic (or endothermic) and release (or absorb) heat.

The heat generation rate from Joule heating $\dot{Q}_J(x,T)$ due to irreversible resistive losses can be expressed as [11,30,32–34],

$$\dot{Q}_J(x,T) = I[V(x,T) - U^{avg}(x,T)]. \tag{5}$$

Here, I is the imposed current, $V(x,T)$ is the cell potential, and $U^{avg}(x,T)$ is the open-circuit voltage evaluated at the volume-average concentration in the cell considering a single electrochemical reaction [35]. In other words, $U^{avg}(x,T)$ is the potential to which the cell would relax if the current was interrupted [32]. It is equivalent to the open-circuit voltage $U_{OCV}(x,T)$ obtained from potentiometric entropy measurements but for current pulses corresponding to the same C-rate as that imposed during galvanostatic cycling in the *operando* isothermal calorimetry measurements of $\dot{Q}_T(x,T)$ [11]. The overpotential $[V(x,T) - U^{avg}(x,T)]$ is the potential drop across the cell due to internal resistance. Therefore, it increases with (i) increasing charge transfer resistance [36], (ii) decreasing ionic conductivity [36], and (iii) increasing cell degradation due to electrode deformation and/or electrolyte decomposition during cycling [37,38].

The reversible heat generation rate $\dot{Q}_{rev}(x,T)$ due to entropic changes can be expressed as [32–34],

$$\dot{Q}_{rev}(x,T) = IT\frac{\partial U^{avg}(x,T)}{\partial T}. \tag{6}$$

In addition, based on Eq. (2), $\dot{Q}_{rev}(x,T)$ can be defined as the sum of the reversible heat generation rates at the $Ti_2Nb_2O_9$ working electrode $\dot{Q}_{rev,TNO}(x,T)$ and at the lithium metal counter electrode $\dot{Q}_{rev,Li}(T)$ such that $\dot{Q}_{rev}(x,T) = \dot{Q}_{rev,TNO}(x,T) + \dot{Q}_{rev,Li}(T)$ with [11],

$$\begin{aligned} &\dot{Q}_{rev,TNO}(x,T) = \frac{IT}{e}\frac{\partial s_{TNO}(x,T)}{\partial x} = \frac{IT}{e}s^{\circ}_{Li}(T) + IT\frac{\partial U^{avg}(x,T)}{\partial T} \\ &\text{and} \quad \dot{Q}_{rev,Li}(T) = -\frac{IT}{e}s^{\circ}_{Li}(T). \end{aligned} \tag{7}$$

However, the reversible heat generation rate is associated not only with entropic changes due to electrochemical reactions [32–34,39] but also with other physicochemical phenomena including ion adsorption/desorption [40–45] and ion solvation/desolvation accompanied by ion-pairing [46–50]. Finally, at extremely small currents, the overpotential and ion concentration gradients in the cell are negligible, and the total heat generation rate is dominated by $\dot{Q}_{rev}(x,T)$ [51].

The heat generation rate from enthalpy of mixing $\dot{Q}_{mix}(x,T)$ due to ion concentration gradients can be expressed as [32–34],

$$\dot{Q}_{mix}(x,T) = \int_{V_\infty}\sum_i\left[\overline{h}_i(x,T) - \overline{h}_i^{avg}(x,T)\right]\frac{\partial c_i}{\partial t}\,\mathrm{d}V \tag{8}$$

where V_∞ is the volume of the cell, $\overline{h}_i(x,T)$ and $\overline{h}_i^{avg}(x,T)$ are respectively the local and the volume-averaged partial molar enthalpy of ion species i, and c_i is the local concentration of ion species i in the electrolyte or the electrode. The heat generation rate from enthalpy of mixing is caused by ion concentration gradients (i) across the electrolyte due to diffusion limitations, (ii) across the electrode due to non-uniform current distribution, (iii) within the pores of the electrode filled with electrolyte, and (iv) among intercalated lithium ions in the electrode due to electrochemical reactions. The latter is typically the dominant contribution [32,35,52]. Therefore, fast lithium ion transport in the electrode reduces the heat generation rate $\dot{Q}_{mix}(x,T)$.

Finally, the heat generation rate due to side reactions $\dot{Q}_{sr}(x,T)$ can be expressed as [32–34],

$$\dot{Q}_{sr}(x,T) = -\sum_i \Delta H_i \dot{r}_i(t) \tag{9}$$

where ΔH_i is the enthalpy of reaction for side reaction i occurring at reaction rate $\dot{r}_i(t)$. However, past studies on heat generation in a battery cell have generally neglected $\dot{Q}_{sr}(x,T)$ [32–34]. Indeed, side reactions usually arise from the ageing process of a battery cell, which is relatively slow unless the cell is operating under extreme conditions [33,34,53]. Therefore, in this study $\dot{Q}_{sr}(x,T)$ was also neglected.

2.3. Energy balance

The net thermal energy Q_i (in J) attributed to the different contributions previously mentioned and released over a charging/discharging cycle can be expressed as [34],

$$Q_i = \oint_{cycle}\dot{Q}_i(x,T,t)\mathrm{d}t \quad \text{with } i = T,\ J,\ \text{or } mix. \tag{10}$$

Note that the reversible heat generation rate $\dot{Q}_{rev}(x,T,t)$ averaged over a cycle yields zero, i.e., $Q_{rev} = 0$.

Moreover, the net electrical energy loss ΔE_e (in J) over a charging/discharging cycle corresponds to the area enclosed by the hysteresis of $V(x,T)$ vs. the charge transferred q such that [54],

$$\Delta E_e = \oint_{cycle} V(x,T)\mathrm{d}q = \oint_{cycle} V(x,T,t)I(t)\mathrm{d}t. \tag{11}$$

According to the first law of thermodynamics, the total thermal energy released during a cycle is equal to the net electrical energy loss such that [11,30],

$$\Delta E_e = Q_T = Q_J + Q_{mix}. \tag{12}$$

3. Materials and methods

3.1. Synthesis of $Ti_2Nb_2O_9$ powder

In this study, $Ti_2Nb_2O_9$ powder was synthesized by either a solid-state or a sol-gel process. In the solid-state synthesis method, powder of Nb_2O_5 (Alfa Aesar, 99.9%), TiO_2 (Alfa Aesar, ≥ 99%), and K_2CO_3 (ACS Reagent, ≥ 99.0%) was mixed with a molar ratio of 1:2:1.2. Here, 20% excess of K_2CO_3 was added owing to its volatility at high temperatures. This mixture was ground in an agate mortar for 10 min to obtain a homogeneous powder. This powder was calcined at 1100 °C in a platinum crucible in air for 12 h to produce $KTiNbO_5$ powder [55,56].

In the sol-gel synthesis method, 1.351 mg of $NbCl_5$ (Sigma Aldrich, 99%) was dissolved in 30 mL of ethanol. Meanwhile, 1.703 mg of titanium isopropoxide (Alfa Aesar, 97%) and 0.370 mg of KCl (ACS Reagent, 99.0–100.5%) were dissolved in 200 mL of ethylene glycol. Then, citric acid (Alfa Aesar, ≥ 99%) was added to this second solution to achieve a molar ratio of 10:1 between citric acid and the total number of cations in both solutions (Nb, Ti, and K). After waiting for 1 h to ensure complete dissolution of all species, the two solutions were mixed, then stirred and heated at 120 °C until a blackish gel was formed. This gel was dehydrated at 300 °C in air overnight so that the organic species completely evaporated. It was then calcined at 700 °C in air for 2 h to produce $KTiNbO_5$ powder. Note that it was necessary to evacuate the chlorinated gases out of the handling room.

The final step, common to both synthesis methods, consisted of mixing and stirring 1 g of the $KTiNbO_5$ powder in 200 mL of 3 M aqueous HNO_3 for 3 days. The acid solution was changed daily to ensure the complete exchange of potassium cations with protons [55]. The resulting suspension containing $HTiNbO_5$ powder was then centrifuged and rinsed with DI water until waste water at neutral pH was obtained. Finally, the dried $HTiNbO_5$ powder was calcined at 400 °C in air for 2 h to obtain $Ti_2Nb_2O_9$ powder synthesized by solid-state or sol-gel methods [13].

3.2. Electrode and device fabrication

A first set of self-supported electrodes were fabricated from a slurry prepared by mixing one of the $Ti_2Nb_2O_9$ powders previously synthesized by solid-state or sol-gel methods with conductive carbon (carbon black, Superior Graphite) and aqueous polytetrafluoroethylene (PTFE, Sigma Aldrich) in a small amount of ethanol with a mass ratio of 7.5:1.5:1. This slurry was homogenized with a pestle in a mortar and then cold-rolled until self-supported electrodes were obtained with mass loading between 4 and 5 mg/cm^2 and thickness between 60 and 75 μm [57]. These self-supported electrodes were used for *in situ* X-ray diffraction (XRD), cyclic voltammetry, galvanostatic cycling, and potentiometric entropy measurements. *In situ* XRD was performed on cells made according to the procedure first reported by Leriche et al. [58] and consisting of (i) a self-supported solid-state or sol-gel $Ti_2Nb_2O_9$ working electrode, (ii) a polished lithium metal (Sigma Aldrich, 99.9%) counter electrode, (iii) a 675 μm thick glass microfiber filter (Whatman, Grade GF/D) as the separator, impregnated with (iv) 1 M $LiPF_6$ in EC:DMC 1:1 w/w (Solvionic, battery grade) electrolyte. Similarly, cyclic voltammetry and galvanostatic cycling measurements were performed on Swagelok cells consisting of (i) a self-supported solid-state or sol-gel $Ti_2Nb_2O_9$ working electrode, (ii) a polished lithium metal (Sigma Aldrich, 99.9%) counter electrode, (iii) a 675 μm thick glass microfiber filter (Whatman, Grade GF/D) as the separator, impregnated with (iv) 1 M $LiPF_6$ in EC:DMC 1:1 w/w (Solvionic, battery grade) electrolyte. Finally, potentiometric entropy measurements at C-rate of C/10 were performed on coin cells consisting of (i) a self-supported solid-state or sol-gel $Ti_2Nb_2O_9$ working electrode, (ii) a polished lithium metal (Sigma Aldrich, 99.9%) counter electrode, (iii) a 260 μm thick glass microfiber filter (Whatman, Grade GF/C) as the separator, impregnated with (iv) 1 M $LiPF_6$ in EC:DMC 1:1 v/v (Sigma Aldrich, battery grade) electrolyte. Here, the *in situ* XRD cells, Swagelok cells, and coin cells were assembled in a glove box containing Ar gas with less than 0.1 ppm of O_2 and H_2O.

Another set of electrodes were fabricated on copper current collectors from a slurry prepared by dispersing one of the $Ti_2Nb_2O_9$ powders previously synthesized by solid-state or sol-gel methods and conductive carbon (carbon black, Superior Graphite) in N-methyl-2-pyrrolidone (NMP) solvent with a $Ti_2Nb_2O_9$:conductive carbon mass ratio of 5:1. After dispersion in the solvent, polyvinylidene fluoride (PVDF) dissolved in NMP (7 wt%) was added to achieve a $Ti_2Nb_2O_9$:PVDF mass ratio of 7.5:1. Next, the slurry was spread on a large copper substrate using a doctor blade and then dried in ambient air overnight. The obtained slurry-cast electrodes had a $Ti_2Nb_2O_9$:conductive carbon:PVDF mass ratio of 7.5:1.5:1, mass loading around 5.5 mg/cm^2, and thickness around 150 μm. These electrodes were used to make two-electrode cells for *operando* isothermal calorimetry. The cells consisted of (i) a slurry-cast solid-state or sol-gel $Ti_2Nb_2O_9$ working electrode and cut into 1 cm × 1 cm square shape, (ii) a polished lithium metal (Sigma Aldrich, 99.9%) counter electrode also cut into 1 cm × 1 cm square shape, (iii) two 50 μm thick polypropylene/polyethylene (Celgard, C380) sheets acting as separators and thermal insulators, impregnated with (iv) 1 M $LiPF_6$ in EC:DMC 1:1 v/v (Sigma Aldrich, battery grade) electrolyte. Similarly, potentiometric entropy measurements at C-rates of 1.5C and 6C were performed on coin cells consisting of (i) a slurry-cast solid-state or sol-gel $Ti_2Nb_2O_9$ working electrode, (ii) a polished lithium metal (Sigma Aldrich, 99.9%) counter electrode, (iii) a 260 μm thick glass microfiber filter (Whatman, Grade GF/C) as the separator, impregnated with (iv) 1 M $LiPF_6$ in EC:DMC 1:1 v/v (Sigma Aldrich, battery grade) electrolyte. Here also, the calorimetric cells and coin cells were assembled in a glove box containing Ar gas with less than 0.1 ppm of O_2 and H_2O.

3.3. Structural characterization

Transmission electron microscopy (TEM) and *in situ* XRD were performed in order to characterize the structure and phases of $Ti_2Nb_2O_9$ powder synthesized by solid-state or sol-gel methods. TEM images were collected using a probe-corrected Themis Z G3 microscope (Thermo Fisher Scientific) equipped with a high-angle annular dark-field detector (Fischione). Here, the $Ti_2Nb_2O_9$ powder was dispersed in ethanol and then deposited on a copper grid. Both the XRD patterns of pristine $Ti_2Nb_2O_9$ powders and the *in situ* XRD patterns of $Ti_2Nb_2O_9$ electrodes were collected using a PANalytical X'Pert Pro diffractometer (Malvern Panalytical). An X'Celerator detector with Cu-K$_{\alpha1}$-K$_{\alpha2}$ ($\lambda = 1.54060$ Å, 1.54439 Å) radiation was used at acceleration voltage of 40 kV and current of 40 mA. During charging and discharging of the cell, a series of constant current pulses at 0.02 A/g of $Ti_2Nb_2O_9$ were imposed. Each current pulse lasted 20 min followed by a relaxation period of 30 min for pattern acquisition between $2\theta = 5^\circ$ and 40°.

3.4. Electrochemical characterization

Cyclic voltammetry measurements consisted of imposing a triangular waveform as the cell potential V and recording the cell current I with a high accuracy potentiostat (BioLogic, VMP3). The specific capacity $C_m(\nu)$ (in mAh/g) at scan rate ν was calculated according to [59],

$$C_m(\nu) = \frac{1}{m}\oint_{cycle}\frac{I}{2\nu}\mathrm{d}V \tag{13}$$

where m is the mass loading of $Ti_2Nb_2O_9$ at the working electrode.

Similarly, the cell potential V under galvanostatic cycling at constant current $\pm I$ was also recorded by a high accuracy potentiostat (BioLogic, VMP3). The IR drop ΔV can be identified as the sharp potential change observed when switching between charging and discharging or vice versa. Then, the internal resistance R_{GC} of the cell was calculated according to [40,60-63],

$$R_{GC} = \frac{\Delta V}{2I}. \tag{14}$$

3.5. Potentiometric entropy measurements

The open-circuit voltage $U_{OCV}(C_m, T)$ and entropic potential $\partial U_{OCV}(C_m, T)/\partial T$ of the coin cells with working electrodes made of $Ti_2Nb_2O_9$ microparticles or nanoparticles synthesized by solid-state or sol-gel methods were measured as functions of specific capacity C_m using the potentiometric entropy measurement technique and the apparatus described in Refs. [11,30]. The measurements consisted of imposing a series of constant current pulses at a C-rate of C/10 at 20 °C. Each current pulse lasted 30 min followed by a relaxation period of 270 min during which a step-like temperature profile was applied to the coin cell from 15 °C to 25 °C in 5 °C increments with a thermoelectric cold plate (TE technology, CP-121). The corresponding coin cell potential evolution was recorded by a high accuracy potentiostat (BioLogic, VSP-300). Before recording the open-circuit voltage $U_{OCV}(C_m, T)$ at a given specific capacity C_m and temperature T, we verified that the coin cell had reached thermodynamic equilibrium by ensuring that (i) the temperature difference between the cold plate and the surface of the coin cell was less than 0.1 °C and (ii) the time rate of change of the open-circuit voltage $\partial U_{OCV}(C_m, T)/\partial t$ was less than 1 mV/h.

3.6. Operando isothermal calorimetry

Operando isothermal calorimetry was performed in the aforementioned two-electrode cells using the apparatus described in Ref. [64]. Here, galvanostatic cycling was imposed using a high accuracy potentiostat (BioLogic, SP-150). Simultaneously, the instantaneous heat generation rates $\dot{Q}_i(t)$ (in mW) at the working electrode made of $Ti_2Nb_2O_9$ microparticles or nanoparticles and at the lithium metal counter electrode were calculated from the instantaneous heat fluxes $q''_i(t)$ (in mW/cm^2) measured by a 1 cm × 1 cm thermoelectric heat flux sensor (greenTEG, gSKIN-XP) in thermal contact with the back of each electrode "i" according to [64],

$$\dot{Q}_i(t) = q''_i(t)A_i = \frac{\Delta V_i(t)}{S_i}A_i \quad \text{with } i = TNO \text{ or } Li. \tag{15}$$

Here, A_i (in cm^2) is the footprint area of the electrode and $\Delta V_i(t)$ (in μV) is the instantaneous voltage difference measured by the heat flux sensor with sensitivity S_i [in μV/(W/cm^2)]. Then, the instantaneous total heat generation rate in the entire calorimetric cell $\dot{Q}_T(t)$ can be expressed as the sum of those at each electrode such that,

$$\dot{Q}_T(t) = \dot{Q}_{TNO}(t) + \dot{Q}_{Li}(t). \tag{16}$$

In addition, the instantaneous heat generation rates $\dot{Q}_i(t)$ at each electrode can be divided into an irreversible $\dot{Q}_{irr,i}(t)$ and a reversible $\dot{Q}_{rev,i}(t)$ contribution such that,

$$\dot{Q}_i(t) = \dot{Q}_{irr,i}(t) + \dot{Q}_{rev,i}(t). \tag{17}$$

To minimize the white noise in the signal from the heat flux sensors, the instantaneous heat generation rates $\dot{Q}_i(t)$ measured at each electrode were averaged over the last three consecutive cycles at any given current I, i.e.,

$$\dot{Q}_i(t) = \frac{1}{3}\sum_{j=1}^{3}\dot{Q}_i[t+(j-1)t_{cd}]. \tag{18}$$

Finally, the time-averaged irreversible heat generation rates $\overline{\dot{Q}}_{irr,i}$ during a charging/discharging cycle can be calculated according to [11, 30],

$$\overline{\dot{Q}}_{irr,i} = \overline{\dot{Q}}_i = \frac{1}{t_{cd}}\oint_{cycle}\dot{Q}_i(t)\mathrm{d}t \quad \text{with } i = TNO \text{ or } Li. \tag{19}$$

Note that $\dot{Q}_{rev,i}(t)$ averaged over a cycle yields zero.

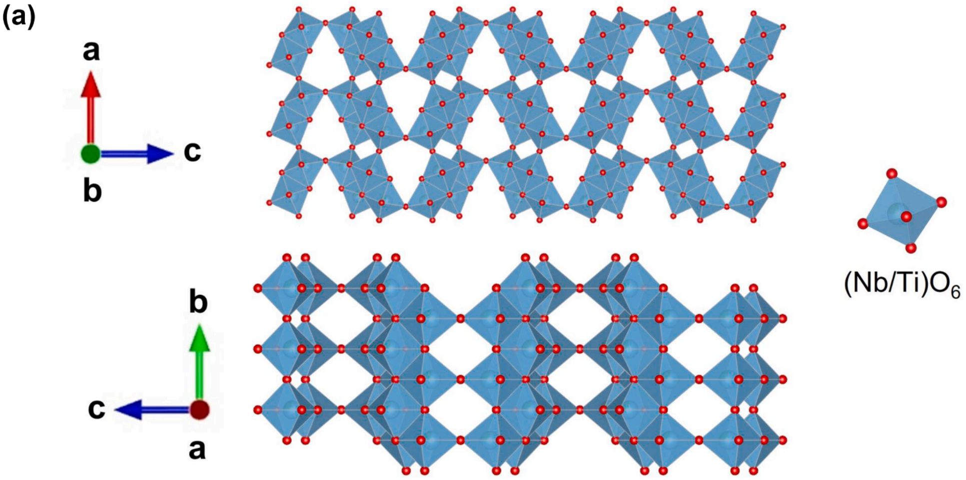

(b) $Ti_2Nb_2O_9$ microparticles synthesized by solid-state method

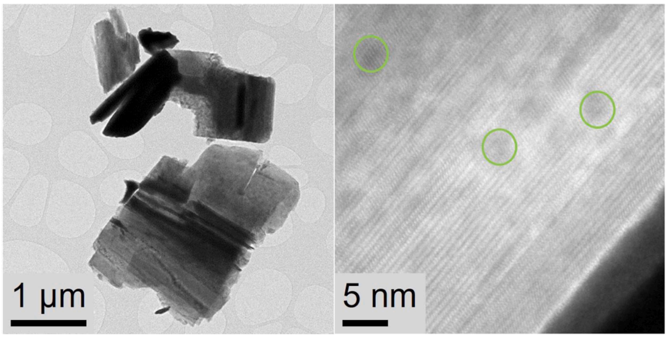

(c) $Ti_2Nb_2O_9$ nanoparticles synthesized by sol-gel method

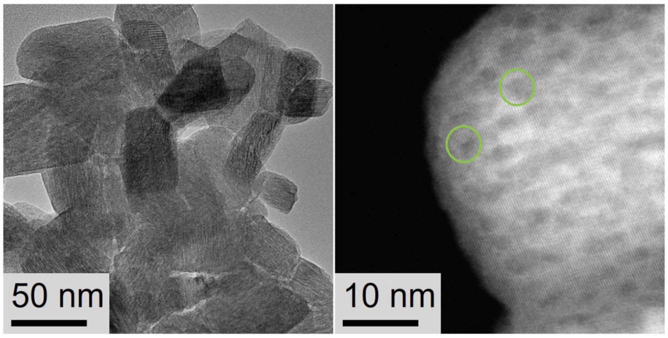

Fig. 1. (a) Crystallographic structure of $Ti_2Nb_2O_9$. Transmission electron microscopy (TEM) images of $Ti_2Nb_2O_9$ (b) microparticles and (c) nanoparticles. Mesopores formed during the dehydration synthesis step are marked by green circles.

4. Results and discussion

4.1. Structural characterization

Fig. 1(a) shows the crystallographic structure of $Ti_2Nb_2O_9$, demonstrating its tunnel structure which facilitates lithium ion intercalation. Figs. 1(b) and 1(c) show the transmission electron microscopy (TEM) images of $Ti_2Nb_2O_9$ microparticles or nanoparticles synthesized by solid-state or sol-gel methods, respectively. Here, the solid-state synthesis method produced microparticles with size around 1 μm while the sol-gel synthesis method produced nanoparticles with size around 50 nm. Furthermore, mesopores formed during the dehydration synthesis step were marked by green circles, showing that the sol-gel method created more nanoporosity in the synthesized $Ti_2Nb_2O_9$ than the solid-state method. In fact, the specific surface area measured by low-temperature nitrogen adsorption porosimetry of $Ti_2Nb_2O_9$ microparticles or nanoparticles reached 1.4 and 24.6 m^2/g, respectively. The respective volumes of micropores and mesopores were 3.16×10^{-5} and 0.0092 cm^3/g in $Ti_2Nb_2O_9$ microparticles, or 0.008 and 0.095 cm^3/g in $Ti_2Nb_2O_9$ nanoparticles. In other words, both types of particles were

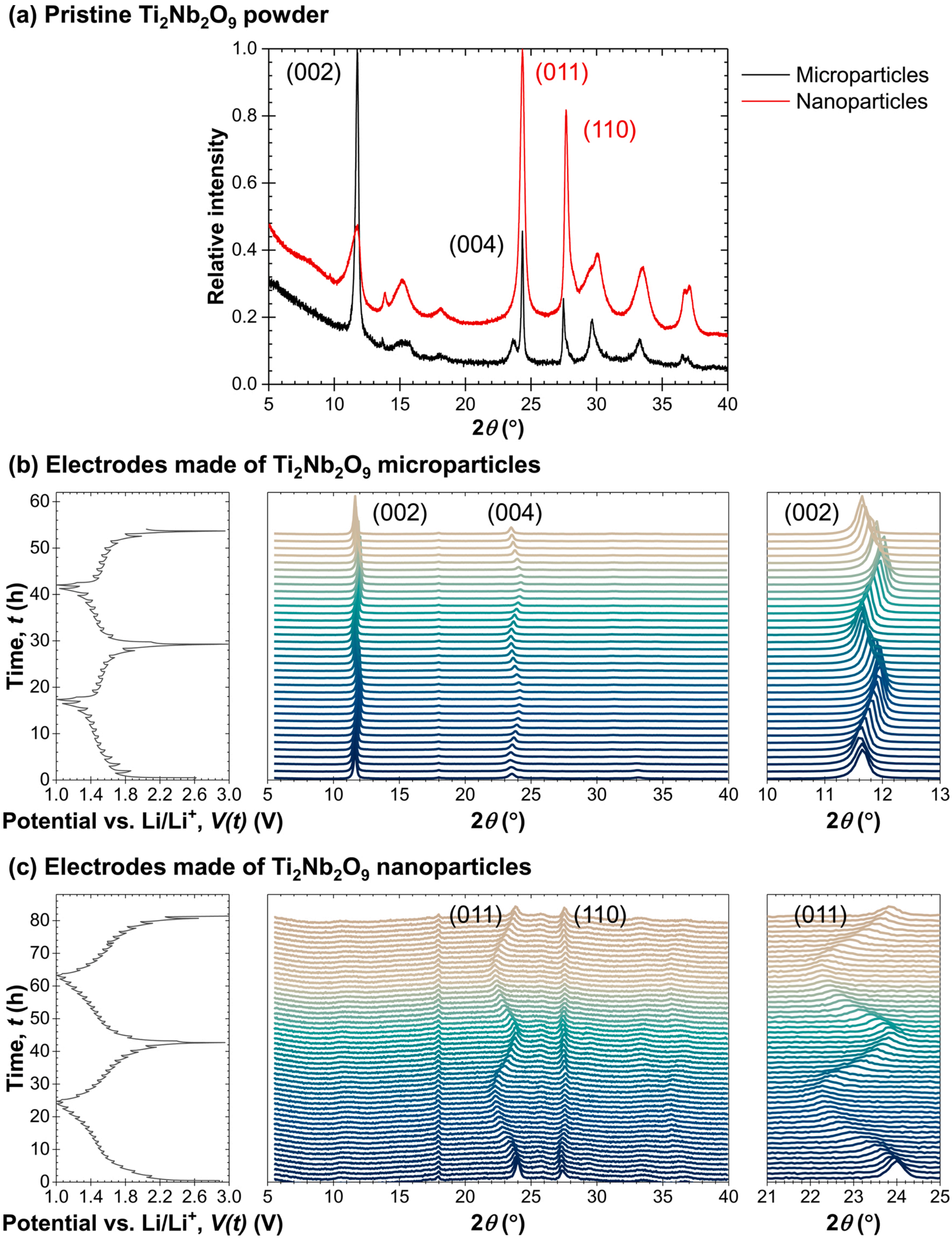

Fig. 2. (a) XRD patterns of pristine $Ti_2Nb_2O_9$ powder. *In situ* XRD patterns of electrodes made of $Ti_2Nb_2O_9$ (b) microparticles or (c) nanoparticles.

dense and slightly porous. The pore size distributions were bimodal with an average pore width of $Ti_2Nb_2O_9$ microparticles and nanoparticles recorded as 17.5 and 4.7 nm, respectively (see Fig. S1 in Supplementary Materials). According to the IUPAC classification [65], the $Ti_2Nb_2O_9$ microparticles contained primarily mesopores with pore width between 2 and 50 nm while the $Ti_2Nb_2O_9$ nanoparticles had nanopores with pore width < 2 nm. Initially for both types of particles, the mesopores were mainly created during the synthesis of the precursor $HTiNbO_5$ while the nanopores were generated mostly due to the final calcination step of $HTiNbO_5$ to obtain $Ti_2Nb_2O_9$.

First, Fig. 2(a) shows the XRD patterns of pristine $Ti_2Nb_2O_9$ powders. Here, $Ti_2Nb_2O_9$ microparticles exhibited preferential orientation along the c-axis based on the high intensity of the (002) and (004) peaks. By contrast, $Ti_2Nb_2O_9$ nanoparticles did not develop preferential growth while the larger peak widths indicate their smaller crystallite size. Furthermore, Fig. 2 shows the *in situ* XRD patterns of self-supported electrodes made of $Ti_2Nb_2O_9$ (b) microparticles or (c) nanoparticles. It indicates that not every expected diffraction peak was observed in the patterns for electrodes made of $Ti_2Nb_2O_9$ microparticles. This was due to (i) the aforementioned preferential orientation of the synthesized $Ti_2Nb_2O_9$ microparticles and (ii) the treatment during synthesis of the powder to form a self-supported paste. Nevertheless, the (002) peak around $2\theta = 12^\circ$ and the (004) peak around $2\theta = 24^\circ$ were clearly visible and could be attributed to $Ti_2Nb_2O_9$ [13,55,66]. Similarly, not every expected diffraction peak was observed for electrodes made of $Ti_2Nb_2O_9$ nanoparticles. This was due to the low crystallinity of the synthesized $Ti_2Nb_2O_9$ nanoparticles. Nonetheless, the (011) peak around $2\theta = 24^\circ$ and the (110) peak around $2\theta = 27^\circ$ were clearly visible and could be attributed to $Ti_2Nb_2O_9$ [13,55,66]. In addition, in both cases the peak around $2\theta = 18^\circ$ did not shift and could be attributed to PTFE in the binder [67]. It is interesting to note that every diffraction peak was maintained at constant intensity and featured small and continuous shifts during lithiation and delithiation which returned to their original position after each cycle. This suggests that the prevailing charging mechanism corresponded to reversible lithium ion insertion in a homogeneous solid solution of $Ti_2Nb_2O_9$ for electrode material synthesized by either method. In other words, the lithiation and delithiation processes caused only minor and reversible distortions to the crystallographic structure of $Ti_2Nb_2O_9$. Finally, the recent study by Drozhzhin et al. [14] reported, during the first lithiation half-cycle, an irreversible phase transformation between two orthorhombic phases within the same space group (Pnmm) along with changes in the unit cell parameters. We hypothesize that this discrepancy possibly appears due to (i) the different specifications of the diffractometers used in the two studies and

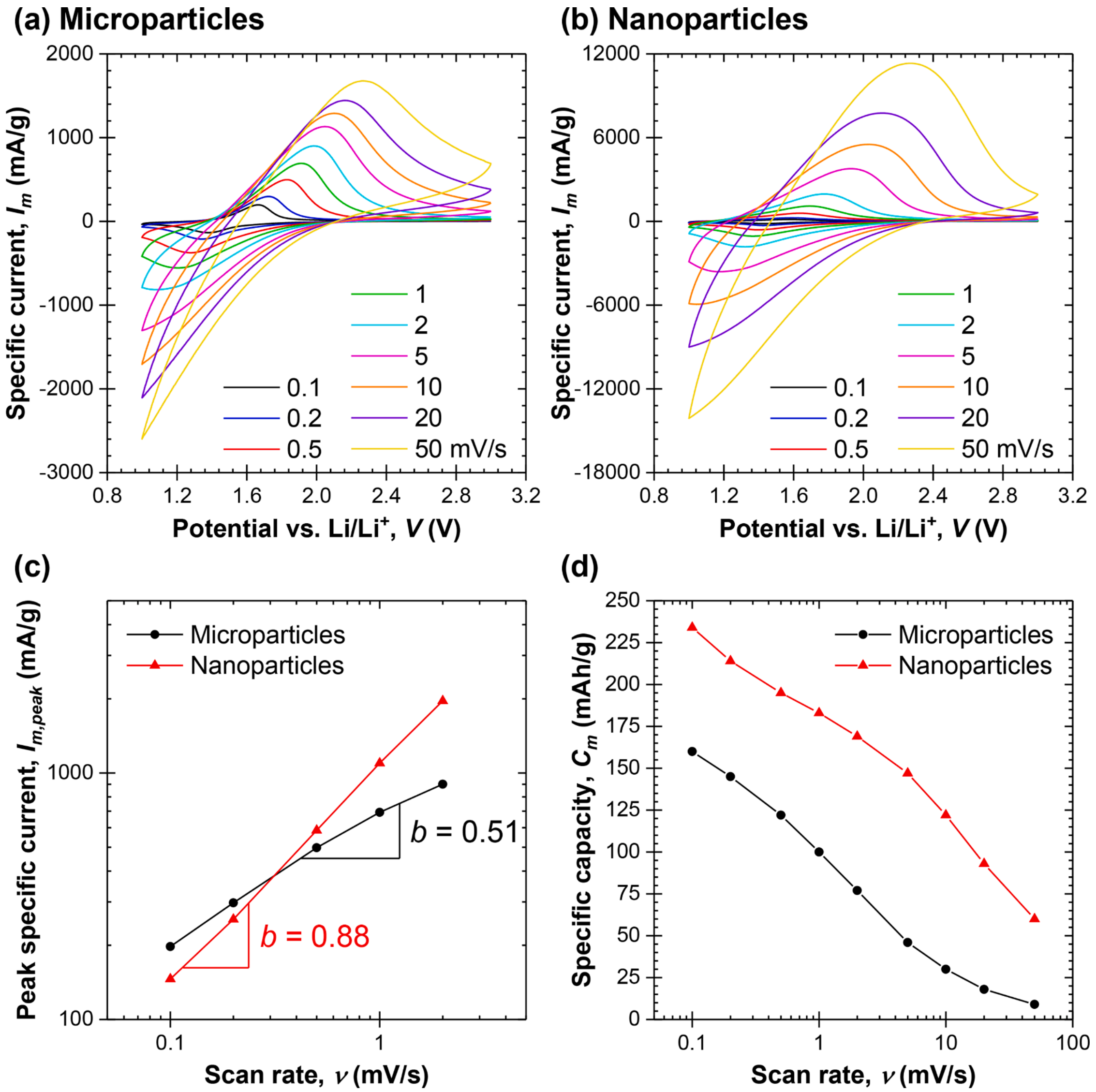

Fig. 3. Cyclic voltammogram of Swagelok cells with working electrodes made of $Ti_2Nb_2O_9$ (a) microparticles or (b) nanoparticles cycled between 1.0 and 3.0 V vs. Li/Li$^+$ at scan rates ν ranging between 0.1 and 50 mV/s, along with (c) peak specific current $I_{m,peak}(\nu)$, and (d) specific capacity $C_m(\nu)$ as functions of scan rate ν.

(ii) differences in the synthesis methods. Indeed, Drozhzhin et al. [14] produced the intermediate compound NH_4TiNbO_5 and the residue NH_3 which potentially created a slight difference in the initial structure. Intercalation in a solid solution was reported for subsequent half-cycles, as observed in the present study.

4.2. *Electrochemical characterization*

Fig. 3 plots the cyclic voltammogram of the Swagelok cells with self-supported working electrodes made of $Ti_2Nb_2O_9$ (a) microparticles or (b) nanoparticles cycled between 1.0 and 3.0 V vs. Li/Li$^+$ at scan rates ν ranging between 0.1 and 50 mV/s. It also shows (c) the peak specific current $I_{m,peak}(\nu)$, and (d) the specific capacity $C_m(\nu)$ as functions of scan rate ν. The pair of cathodic and anodic peaks around 1.4/1.6 V vs. Li/Li$^+$, observed at $\nu = 0.1$ mV/s, could be attributed to both Ti^{4+}/Ti^{3+} and Nb^{5+}/Nb^{4+} redox reactions [13,68,69]. At any given scan rate ν, the polarization of the cell with $Ti_2Nb_2O_9$ nanoparticles was smaller than that with $Ti_2Nb_2O_9$ microparticles. This resulted in greater cycling reversibility for the cell with $Ti_2Nb_2O_9$ nanoparticles than that with $Ti_2Nb_2O_9$ microparticles. Moreover, the b-value associated with this pair of redox peaks was obtained by least squares fitting of the peak specific current $I_{m,peak}$ according to the power law $I_{m,peak} = a\nu^b$ [70]. Note that the b-value analysis is a qualitative technique widely used to assess the charging mechanisms in both battery and pseudocapacitive electrode materials ranging between the limiting cases of slow redox reactions limited by ion diffusion in a semi-infinite medium (b = 0.5) and fast redox reactions without ion transport limitation (b = 1). In fact, a series of studies [71,72] validated the b-value analysis in hybrid pseudocapacitors using state-of-the-art numerical simulations and physicochemical models based on first principles. Between $\nu = 0.1$ and 2 mV/s, the b-value of the cell with $Ti_2Nb_2O_9$ microparticles or nanoparticles was 0.51 and 0.88, respectively. This suggests that redox reactions and lithium ion intercalation were faster and less diffusion-limited in the working electrode made of $Ti_2Nb_2O_9$ nanoparticles than that made of $Ti_2Nb_2O_9$ microparticles thanks to their larger surface area and smaller size. Finally, at any given scan rate ν, the specific capacity $C_m(\nu)$ of the cell with $Ti_2Nb_2O_9$ nanoparticles was larger than that with $Ti_2Nb_2O_9$ microparticles. In addition, the decrease in the specific capacity $C_m(\nu)$

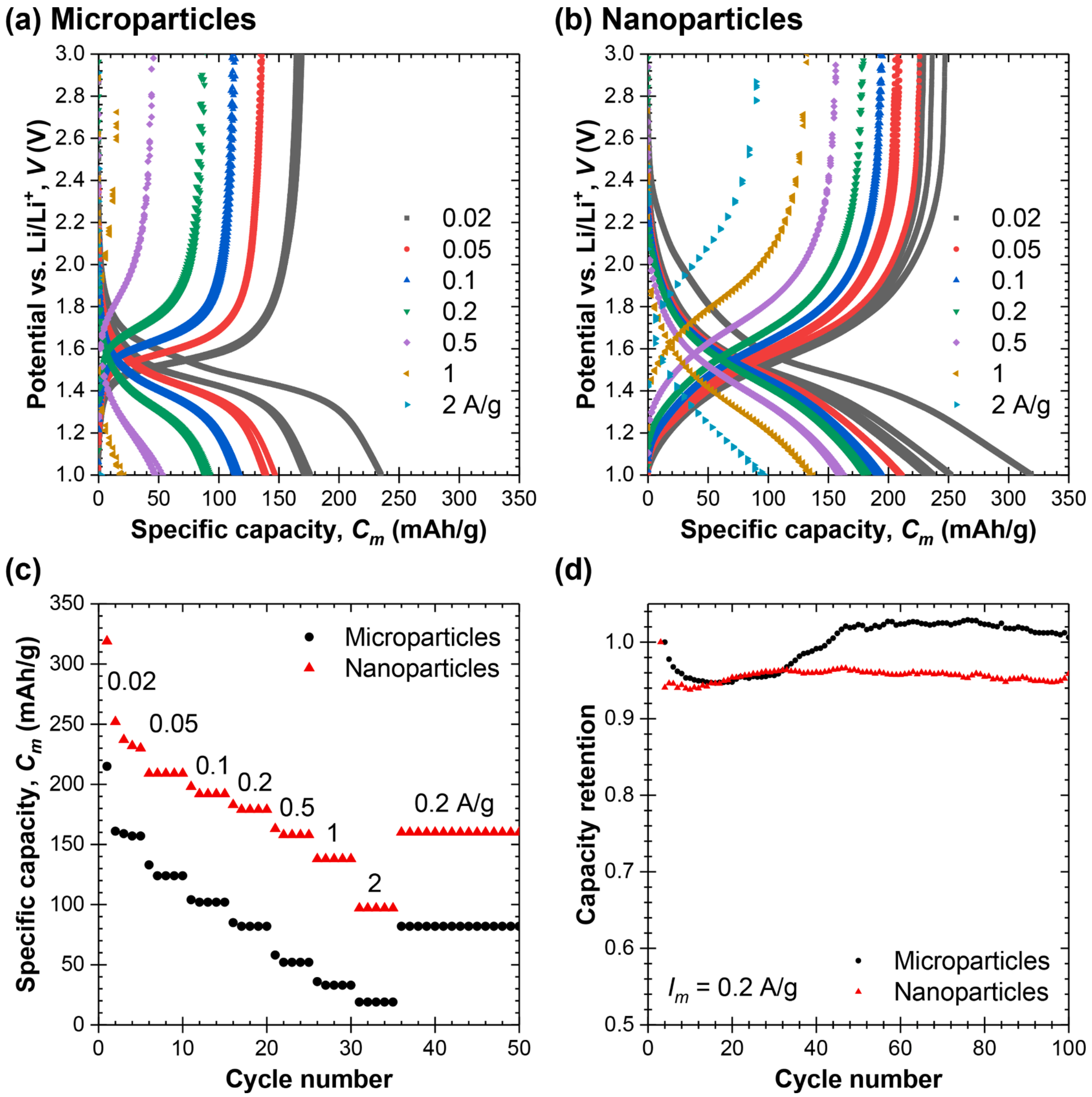

Fig. 4. Potential profiles during galvanostatic cycling of Swagelok cells with working electrodes made of $Ti_2Nb_2O_9$ (a) microparticles or (b) nanoparticles cycled between 1.0 and 3.0 V vs. Li/Li$^+$ at specific current I_m ranging between 0.02 and 2 A/g of $Ti_2Nb_2O_9$, along with (c) the specific capacity $C_m(I_m)$ as a function of cycle number at different specific current I_m, and (d) the capacity retention ratio over 100 cycles with respect to $C_m(I_m)$ of the second cycle at $I_m = 0.2$ A/g of $Ti_2Nb_2O_9$ (~1C).

with increasing scan rate ν was less significant for the cell with $Ti_2Nb_2O_9$ nanoparticles than that with $Ti_2Nb_2O_9$ microparticles.

Fig. 4 plots the potential profiles during galvanostatic cycling of the Swagelok cells with self-supported working electrodes made of $Ti_2Nb_2O_9$ (a) microparticles or (b) nanoparticles cycled between 1.0 and 3.0 V vs. Li/Li^+ at specific current I_m ranging between 0.02 and 2 A/g of $Ti_2Nb_2O_9$. It also shows (c) the specific capacity $C_m(I_m)$ as a function of cycle number at different specific current I_m, and (d) the capacity retention ratio over 100 cycles with respect to $C_m(I_m)$ of the second cycle at $I_m = 0.2$ A/g of $Ti_2Nb_2O_9$ ($\sim$1C). At any given specific current I_m, the specific capacity $C_m(I_m)$ of the cell with $Ti_2Nb_2O_9$ nanoparticles was larger than that with $Ti_2Nb_2O_9$ microparticles. For example, at 0.02 A/g of $Ti_2Nb_2O_9$ ($\sim$C/10), the cell with $Ti_2Nb_2O_9$ nanoparticles showed a reversible specific capacity of 230 mAh/g compared with 157 mAh/g for the cell with $Ti_2Nb_2O_9$ microparticles. The former achieved an improvement of 14% over the specific capacity previously reported in the literature [13,14]. Moreover, at large specific currents I_m, the capacity retention of the cell with $Ti_2Nb_2O_9$ nanoparticles was superior to that with $Ti_2Nb_2O_9$ microparticles. In fact, at 2 A/g of $Ti_2Nb_2O_9$ ($\sim$10C), the cell with $Ti_2Nb_2O_9$ nanoparticles still retained a specific capacity of 97 mAh/g compared with 19 mAh/g for the cell with $Ti_2Nb_2O_9$ microparticles. Finally, the long-term cycling degradation of both types of $Ti_2Nb_2O_9$ working electrodes was minimal. After 100 cycles at 0.2 A/g of $Ti_2Nb_2O_9$, the ratio of the specific capacity of the cell with $Ti_2Nb_2O_9$ microparticles or nanoparticles relative to the second cycle was 1.01 and 0.96, respectively. Note that in many battery electrode materials such as graphite and NMC, the first cycle features low coulombic efficiency and/or substantial irreversible loss in the specific capacity [73]. Accordingly, it is more appropriate to use the specific capacity of the second cycle as the reference when calculating the capacity retention [74–76].

4.3. Potentiometric entropy measurements

Fig. 5 plots the open-circuit voltage $U_{OCV}(C_m, T)$ and entropic potential $\partial U_{OCV}(C_m, T)/\partial T$ of the coin cells with self-supported working electrodes made of $Ti_2Nb_2O_9$ microparticles or nanoparticles as functions of specific capacity C_m during lithiation and delithiation of the first two cycles at C-rate of C/10. Here, the $Ti_2Nb_2O_9$ active material mass loading of the cell with $Ti_2Nb_2O_9$ microparticles or nanoparticles was 4.7 and 4.3 mg/cm^2, respectively. First, within the same potential window of 1.0 to 3.0 V vs. Li/Li^+, the maximum specific capacity of the

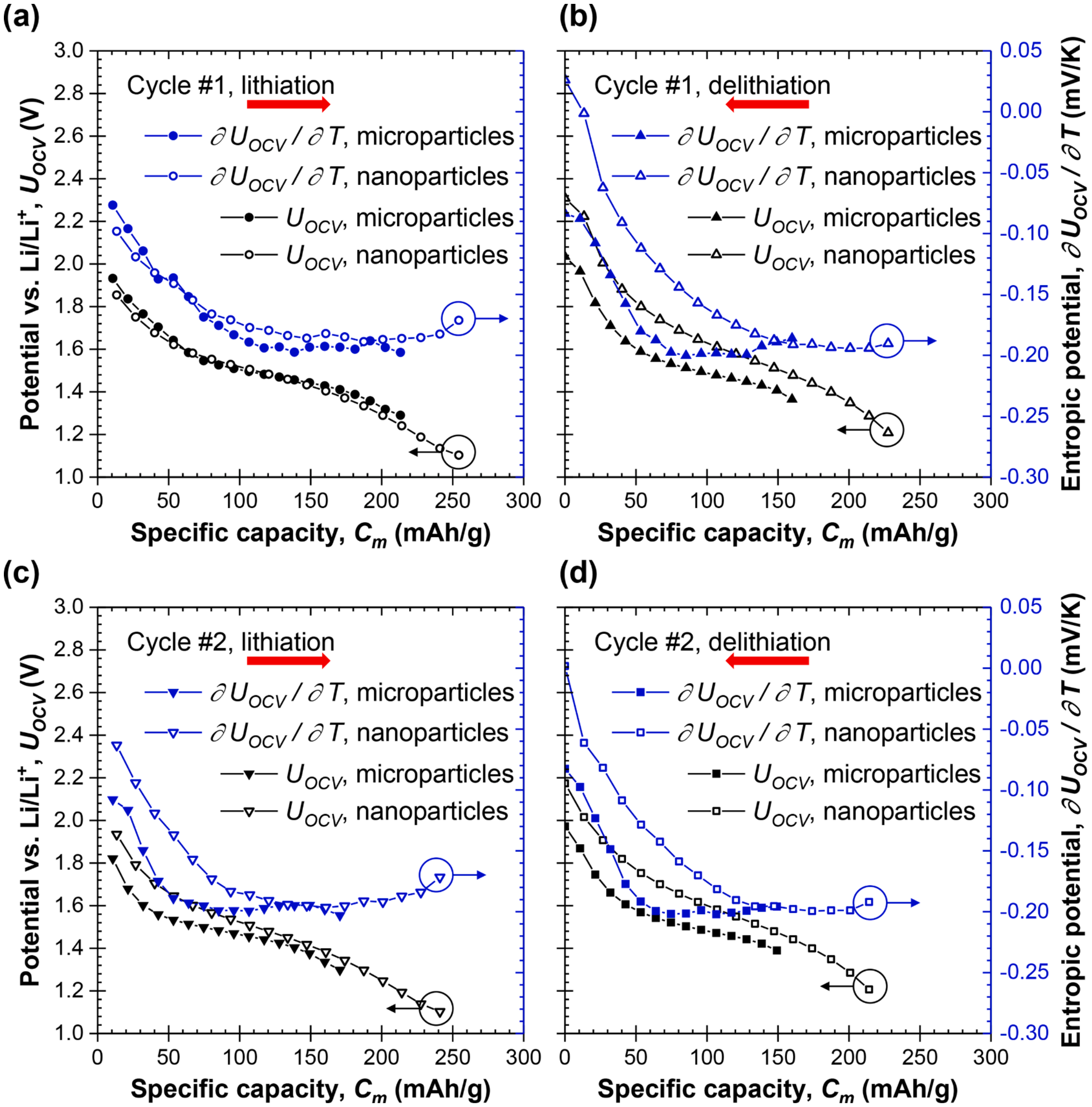

Fig. 5. Open-circuit voltage $U_{OCV}(C_m, T)$ and entropic potential $\partial U_{OCV}(C_m, T)/\partial T$ of coin cells with working electrodes made of $Ti_2Nb_2O_9$ microparticles or nanoparticles as functions of specific capacity C_m during lithiation and delithiation of the first two cycles at C-rate of C/10.

cell with $Ti_2Nb_2O_9$ nanoparticles was larger than that with $Ti_2Nb_2O_9$ microparticles during both lithiation or delithiation half-cycles. These results are consistent with those previously observed in galvanostatic cycling measurements (Fig. 4). Second, $U_{OCV}(C_m, T)$ and $\partial U_{OCV}(C_m, T) / \partial T$ of both cells monotonously decreased with increasing lithium composition during the lithiation half-cycle. This behavior is characteristic of lithium ion insertion in a homogeneous solid solution [11,30]. These observations are also consistent with those previously made from *in situ* XRD measurements (Fig. 2).

Furthermore, $U_{OCV}(C_m, T)$ and $\partial U_{OCV}(C_m, T)/\partial T$ of both cells were the same during the first lithiation half-cycle. This suggests that for pristine $Ti_2Nb_2O_9$, the contrasting particle sizes resulting from distinct synthesis methods had no influence on the thermodynamics properties of the electrodes. However, $U_{OCV}(C_m, T)$ and $\partial U_{OCV}(C_m, T)/\partial T$ between the two cells showed minor discrepancies during the subsequent delithiation half-cycle which could be attributed to several factors. First, it could result from the hysteresis of $U_{OCV}(C_m, T)$ and $\partial U_{OCV}(C_m, T) / \partial T$ between lithiation and delithiation. Moreover, it could be caused by the specific capacity loss between the first lithiation and delithiation half-cycles. On the one hand, such initial specific capacity loss could arise when certain lithium ions lithiated into the pristine structure became trapped and therefore unable to be delithiated [77]. On the other hand, it could also emerge due to increasing kinetic barriers including (i) growing passivation layers on both working and counter electrodes which inhibit lithium ion transport and (ii) broken or cracked $Ti_2Nb_2O_9$ particles which reduce the number of available intercalation sites [78]. For example, cracking can affect the grain boundaries along which electronic and ionic transports occur [79,80]. In fact, a more recent study [81] applied *operando* optical scattering microscopy to monitor the actual process of particle cracking in anode materials leading to nonfunctional particle fragments and degradation of performance caused by the loss of electrical connection to the rest of the electrode.

As previously proposed by Hudak et al. [78], Fig. 6(a) plots the entropic potential $\partial U_{OCV}(C_m, T)/\partial T$ of the coin cells with working electrodes made of $Ti_2Nb_2O_9$ microparticles or nanoparticles as a function of open-circuit voltage $U_{OCV}(C_m, T)$ during lithiation and delithiation of the first two cycles at C-rate of C/10. Here, the entropic potential profiles of both types of electrodes overlapped. This suggests that the

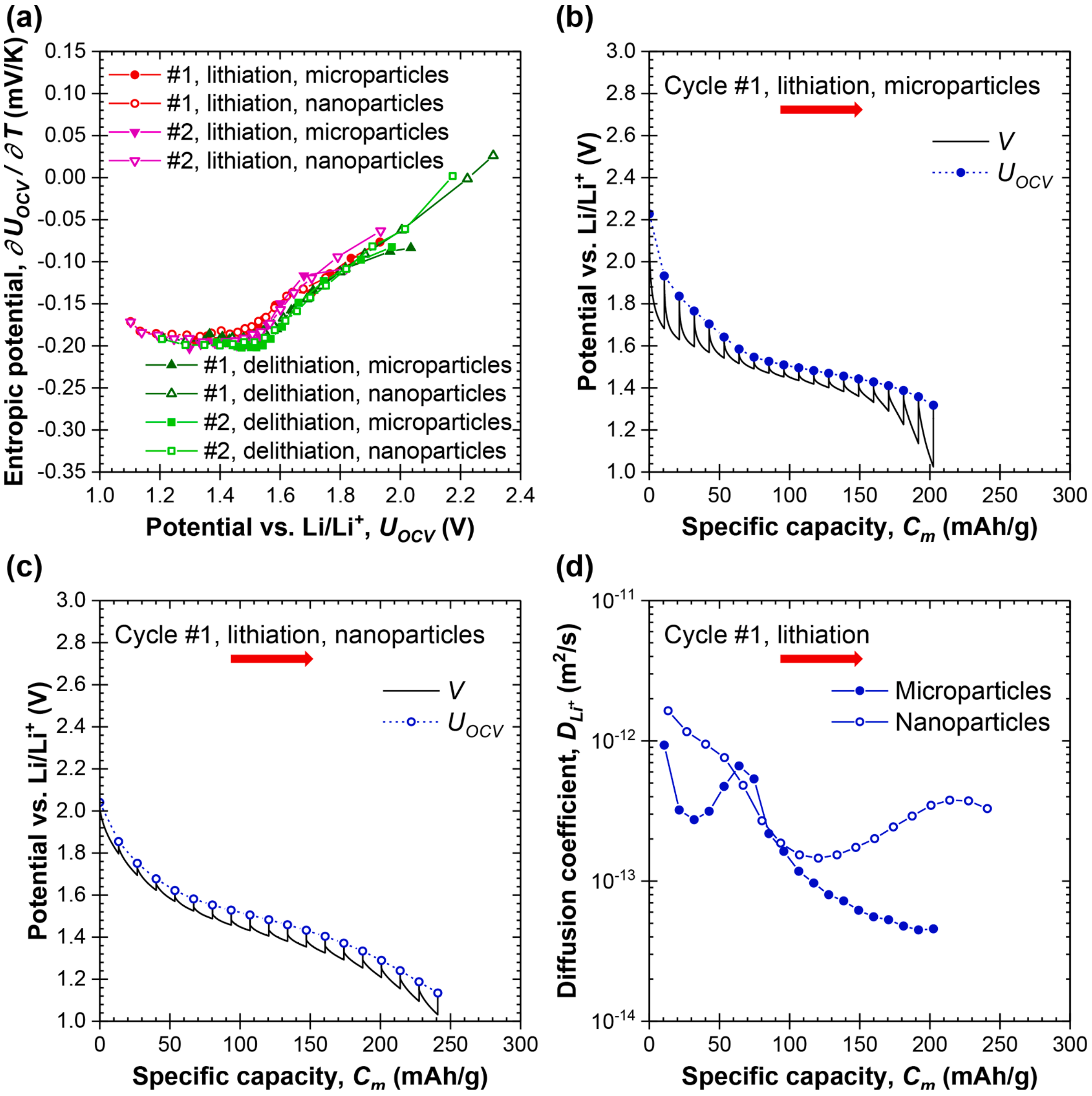

Fig. 6. (a) Entropic potential $\partial U_{OCV}(C_m, T)/\partial T$ of coin cells with working electrodes made of $Ti_2Nb_2O_9$ microparticles or nanoparticles as a function of open-circuit voltage $U_{OCV}(C_m, T)$ during lithiation and delithiation of the first two cycles at C-rate of C/10. Cell potential $V(C_m, T)$ and open-circuit voltage $U_{OCV}(C_m, T)$ as functions of specific capacity C_m during the first lithiation half-cycle at C-rate of C/10 for coin cells with working electrodes made of $Ti_2Nb_2O_9$ (b) microparticles or (c) nanoparticles. (d) Apparent diffusion coefficient $D_{Li^+}(C_m, T)$ [Eq. (3)] of lithium ions in the working electrodes made of $Ti_2Nb_2O_9$ microparticles or nanoparticles.

thermodynamics behavior of $Ti_2Nb_2O_9$ powder synthesized by either method remained similar and stable, at least during the first two cycles. Therefore, the aforementioned minor discrepancies in $U_{OCV}(C_m, T)$ and $\partial U_{OCV}(C_m, T)/\partial T$ vs. C_m between the two cells could be attributed to the lithiation/delithiation hysteresis of $U_{OCV}(C_m, T)$ and $\partial U_{OCV}(C_m, T)\ /\partial T$ as well as the initial specific capacity loss from trapped lithium ions and/or increasing kinetic barriers.

Moreover, Figs. 6(b) and 6(c) plot the cell potential $V(C_m, T)$ and open-circuit voltage $U_{OCV}(C_m, T)$ as functions of specific capacity C_m during the first lithiation half-cycle at C-rate of C/10 for the coin cells with working electrodes made of $Ti_2Nb_2O_9$ microparticles or nanoparticles, respectively. It is evident that, for a given state of charge, the overpotential $[V(C_m, T) - U_{OCV}(C_m, T)]$ of the cell with $Ti_2Nb_2O_9$ nanoparticles was smaller than that with $Ti_2Nb_2O_9$ microparticles. This indicates that the working electrode made of $Ti_2Nb_2O_9$ nanoparticles had larger electrical conductivity and/or faster lithium ion transport than that made of $Ti_2Nb_2O_9$ microparticles [36].

Finally, Fig. 6(d) plots the apparent diffusion coefficient $D_{Li^+}(C_m, T)$ of lithium ions in the working electrodes made of $Ti_2Nb_2O_9$ microparticles or nanoparticles calculated according to Eq. (3). It indicates that, for a given state of charge, $D_{Li^+}(C_m, T)$ of the working electrode made of $Ti_2Nb_2O_9$ nanoparticles was larger than that made of $Ti_2Nb_2O_9$ microparticles, particularly in the second part of the lithiation process. This result confirms the faster lithium ion transport in $Ti_2Nb_2O_9$ nanoparticles compared with microparticles, which manifested itself in the less polarized cyclic voltammograms, the larger b-value, and the larger specific capacity C_m at high C-rates (Figs. 3 and 4).

4.4. Operando isothermal calorimetry

4.4.1. Cell potential

Fig. S2 in Supplementary Materials plots the temporal evolution of the potential $V(t)$ of the calorimetric cells with slurry-cast working electrodes made of $Ti_2Nb_2O_9$ (a) microparticles or (b) nanoparticles and lithium metal counter electrodes for six consecutive galvanostatic cycles with potential window between 1.0 and 3.0 V vs. Li/Li$^+$ for each current I ranging from 2 to 8 mA. It indicates that the cycle period t_{cd} of both cells decreased with increasing current I. In fact, larger currents I led not only to faster charging and discharging rates but also to smaller specific capacity C_m, as observed in Fig. 4. Furthermore, the cycle period t_{cd} of

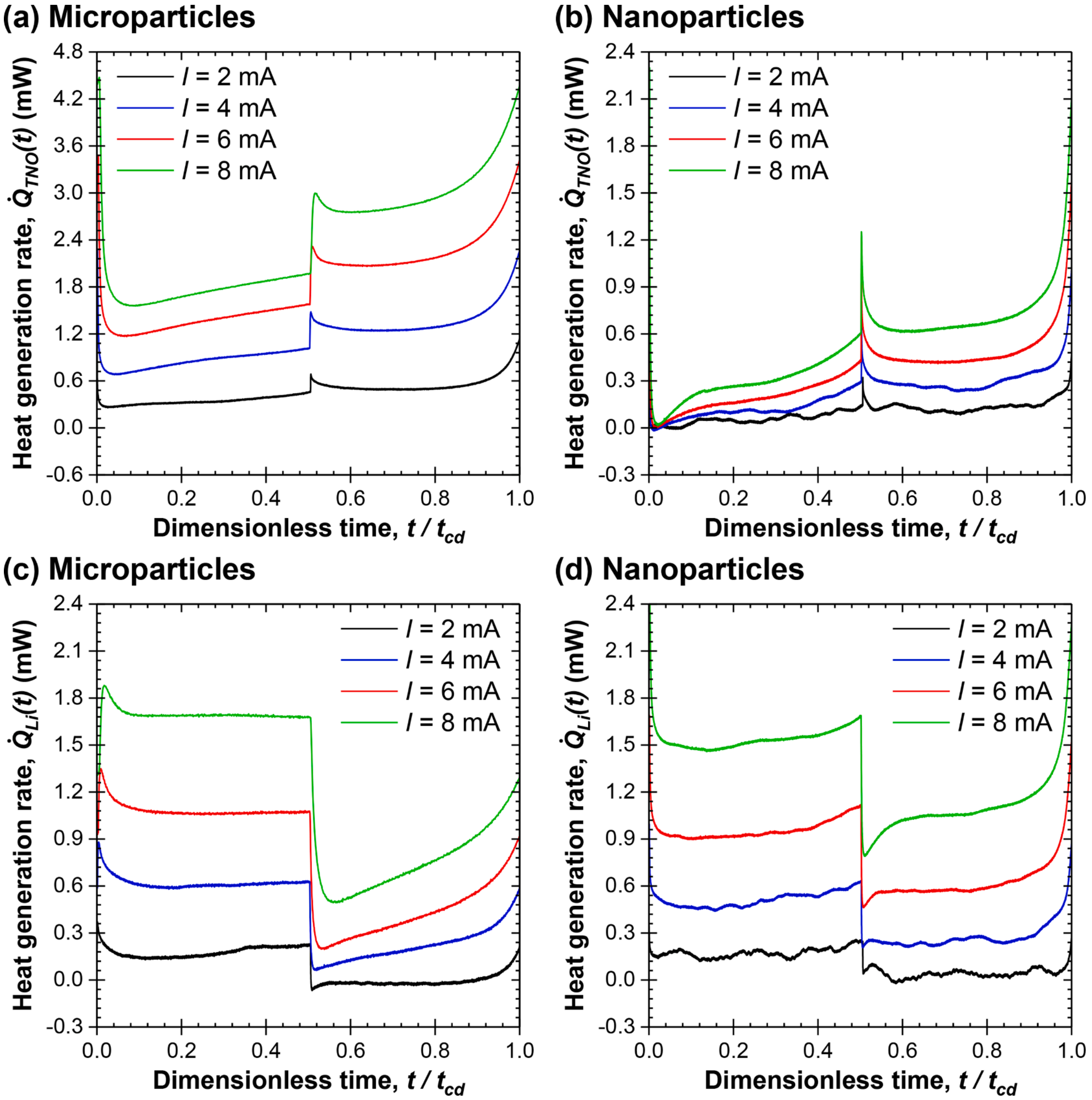

Fig. 7. Instantaneous heat generation rates (a, b) $\dot{Q}_{TNO}(t)$ measured at the working electrodes made of $Ti_2Nb_2O_9$ microparticles or nanoparticles and (c, d) $\dot{Q}_{Li}(t)$ measured at the corresponding lithium metal counter electrodes as functions of dimensionless time t/t_{cd} averaged over the last three consecutive cycles for current I ranging from 2 to 8 mA.

the cell with $Ti_2Nb_2O_9$ nanoparticles was longer than that with $Ti_2Nb_2O_9$ microparticles and did not decrease as much with increasing current I. This reflects the larger specific capacity C_m and the better capacity retention of the cell with $Ti_2Nb_2O_9$ nanoparticles compared with the cell with $Ti_2Nb_2O_9$ microparticles.

4.4.2. *Instantaneous heat generation rates*

Fig. 7 plots the instantaneous heat generation rates (a, b) $\dot{Q}_{TNO}(t)$ measured at the working electrodes made of $Ti_2Nb_2O_9$ microparticles or nanoparticles and (c, d) $\dot{Q}_{Li}(t)$ measured at the respective lithium metal counter electrodes as functions of dimensionless time $t\ /t_{cd}$ averaged over the last three consecutive cycles for current I ranging from 2 to 8 mA. Note that the measurements of $\dot{Q}_{TNO}(t)$ and $\dot{Q}_{Li}(t)$ were repeatable cycle after cycle (see Figs. S3 and S4 in Supplementary Materials). First, the magnitudes of $\dot{Q}_{TNO}(t)$ and $\dot{Q}_{Li}(t)$ in both cells increased with increasing current I. Moreover, Figs. 7(a) and 7(b) show that, for any given current I, $\dot{Q}_{TNO}(t)$ was significantly larger at the working electrode made of $Ti_2Nb_2O_9$ microparticles than at that made of $Ti_2Nb_2O_9$ nanoparticles. Furthermore, $\dot{Q}_{TNO}(t)$ in both cells increased with time during both lithiation or delithiation half-cycles. This could be attributed to the increase in the reversible heat generation rate $\dot{Q}_{rev,TNO}(x,T)$ [Eq. (7)] caused by the monotonously decreasing entropic potential $\partial U_{OCV}(C_m,T)/\partial T$ with increasing lithium composition x, as observed in Fig. 5. On the other hand, Figs. 7(c) and 7(d) establish that, for any given current I, $\dot{Q}_{Li}(t)$ was similar in both cells and was positive and relatively constant during the lithiation half-cycle of the $Ti_2Nb_2O_9$ working electrode. This was associated with lithium ion stripping and exothermic solvation with ion pairing at the lithium metal counter electrode [11]. By contrast, $\dot{Q}_{Li}(t)$ increased towards the end of the delithiation half-cycle of the $Ti_2Nb_2O_9$ working electrode accompanied simultaneously by plating of the lithium metal counter electrode. As such, the rise in $\dot{Q}_{Li}(t)$ could be attributed to the exothermic dendrite formation on the surface of the lithium metal counter electrode [82,83]. These phenomena were also observed in cells with PNb_9O_{25} working electrodes and lithium metal counter electrodes in 1 M $LiPF_6$ in EC:DMC 1:1 v/v electrolyte [11].

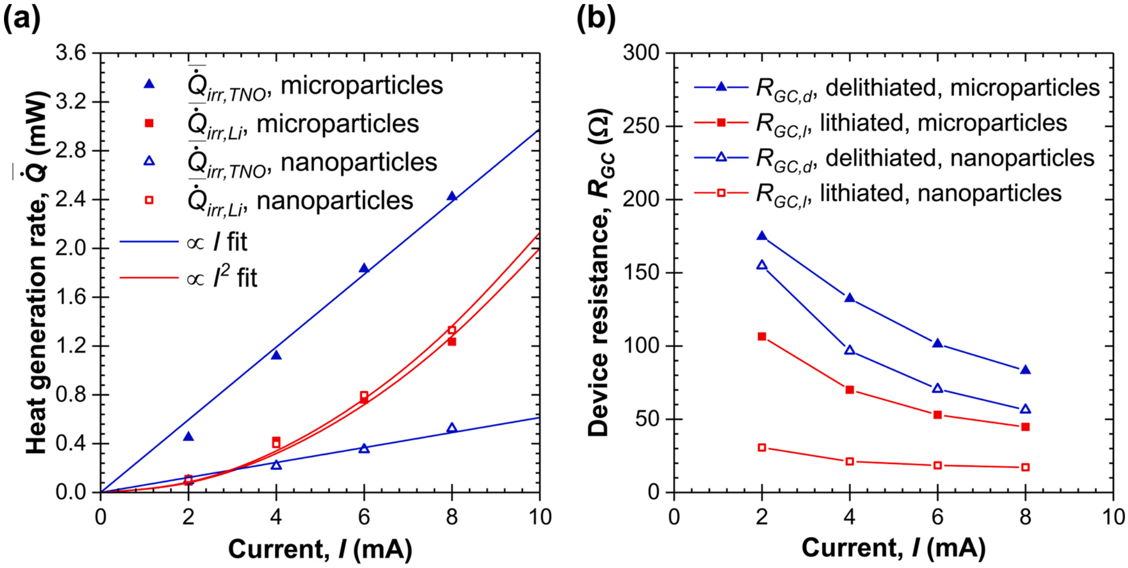

(c) Microparticles

(d) Nanoparticles

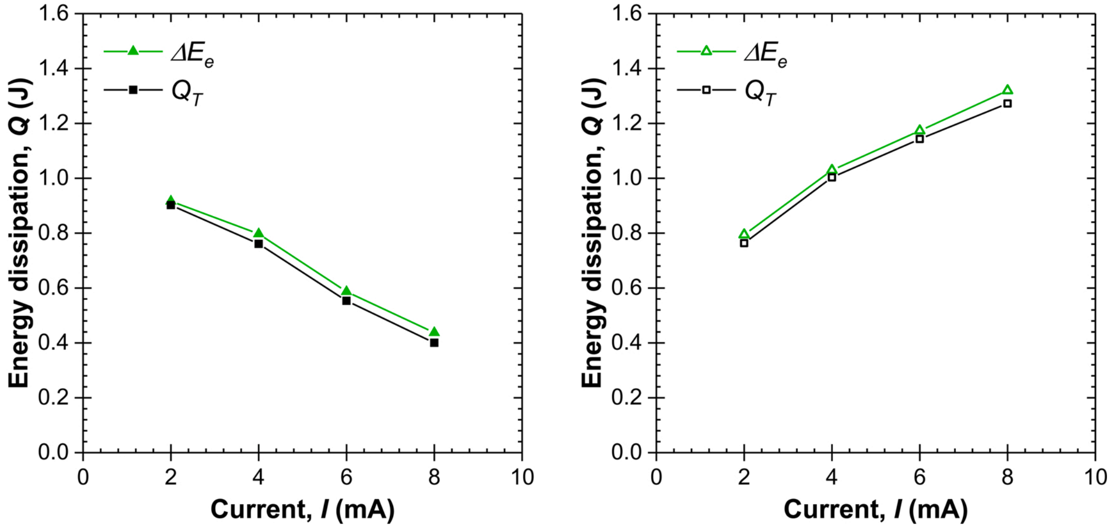

Fig. 8. (a) Time-averaged irreversible heat generation rates $\bar{\dot{Q}}_{irr,TNO}$ and $\bar{\dot{Q}}_{irr,Li}$ as functions of current I for calorimetric cells with working electrodes made of $Ti_2Nb_2O_9$ microparticles or nanoparticles. (b) Resistances $R_{GC,d}$ and $R_{GC,l}$ [Eq. (14)] of calorimetric cells with working electrodes made of $Ti_2Nb_2O_9$ microparticles or nanoparticles in delithiated or lithiated states during cycling at a given current I. Net electrical energy loss ΔE_e [Eq. (11)] and total thermal energy dissipated Q_T [Eq. (10)] over a charging/discharging cycle for calorimetric cells with working electrodes made of $Ti_2Nb_2O_9$ (c) microparticles or (d) nanoparticles.

In our previous studies with $TiNb_2O_7$ [30] and PNb_9O_{25} [11], the heat generation rate $\dot{Q}_J(x,T)+\dot{Q}_{rev}(x,T)$ calculated according to Eqs. (5) and (6) agreed well with the measurements of $\dot{Q}_T(x,T)$. However, in the present study, such a comparison was not possible. Indeed, during *operando* isothermal calorimetry, the cells were tested under galvanostatic cycling at high C-rates resulting in poor capacity retention. However, the values of $U_{OCV}(C_m,T)$ and $\partial U_{OCV}(C_m,T)/\partial T$ determined by potentiometric entropy measurements with current pulses at the same high C-rates spanned a wider range of specific capacity C_m thanks to the long relaxation periods imposed during the measurements (see Figs. S5 to S9 in Supplementary Materials). Therefore, the measured $U_{OCV}(C_m,T)$ and $\partial U_{OCV}(C_m,T)/\partial T$ did not represent the actual values of $U^{avg}(x,T)$ and $\partial U^{avg}(x,T)/\partial T$ of the cells during *operando* isothermal calorimetry.

4.4.3. Time-averaged heat generation rates

Fig. 8(a) plots the time-averaged irreversible heat generation rates $\overline{\dot{Q}}_{irr,TNO}$ and $\overline{\dot{Q}}_{irr,Li}$ as functions of current I for calorimetric cells with working electrodes made of $Ti_2Nb_2O_9$ microparticles or nanoparticles. First, $\overline{\dot{Q}}_{irr,TNO}$ and $\overline{\dot{Q}}_{irr,Li}$ in both cells increased with increasing current I. In fact, least squares fitting revealed that $\overline{\dot{Q}}_{irr,Li}$ increased quadratically with respect to current I, i.e., $\overline{\dot{Q}}_{irr,Li}\propto I^2$. This suggests that Joule heating dominated the irreversible heat generation at the lithium metal counter electrode whose electrical resistivity was independent of current I. Furthermore, for any given current I, $\overline{\dot{Q}}_{irr,Li}$ was identical in both cells. Indeed, each lithium metal counter electrode was cut from the same piece into the same size and therefore should have approximately the same resistance.

By contrast, in both calorimetric cells $\overline{\dot{Q}}_{irr,TNO}$ increased linearly with respect to current I, i.e., $\overline{\dot{Q}}_{irr,TNO}\propto I$. However, $\overline{\dot{Q}}_{irr,TNO}$ was larger at the working electrode made of $Ti_2Nb_2O_9$ microparticles than at that made of $Ti_2Nb_2O_9$ nanoparticles. This could be due, in part, to the fact that the electrical resistivity of the working electrode made of $Ti_2Nb_2O_9$ microparticles was larger than that made of $Ti_2Nb_2O_9$ nanoparticles. In fact, Fig. 8(b) plots the resistances $R_{GC,d}$ and $R_{GC,l}$ calculated from the IR drop [Eq. (14)] in the calorimetric cells with working electrodes made of $Ti_2Nb_2O_9$ microparticles or nanoparticles at the end of the delithiation or lithiation steps during cycling at a given current I. First, the resistances $R_{GC,d}$ and $R_{GC,l}$ of the cell with $Ti_2Nb_2O_9$ microparticles were systematically larger than that with $Ti_2Nb_2O_9$ nanoparticles for any given current I. Moreover, the resistances $R_{GC,d}$ and $R_{GC,l}$ of both cells decreased with increasing current I. This could be attributed to the smaller range of lithium composition x reached at larger currents I. Finally, both cells had larger resistance in delithiated state than in lithiated state, i.e., $R_{GC,d}>R_{GC,l}$. To the best of our knowledge, the electrical resistivity of $Ti_2Nb_2O_9$ as a function of state of charge has not been reported to date. However, the closely-related $TiNb_2O_7$ is known to be an insulator in its unlithiated state and its resistivity decreases sharply upon lithiation up to $x=0.5$ [30]. Thus, a similar behavior could be the origin of the changes in the electrical resistivity of the $Ti_2Nb_2O_9$-based electrodes.

4.4.4. Energy balance

Fig. 8 plots the net electrical energy loss ΔE_e [Eq. (11)] and the total thermal energy dissipated Q_T [Eq. (10)] over a charging/discharging cycle for calorimetric cells with working electrodes made of $Ti_2Nb_2O_9$ (c) microparticles or (d) nanoparticles. For the cell with $Ti_2Nb_2O_9$ microparticles, the total thermal energy Q_T (in J) released over a cycle decreased with increasing current I. This was due to the decrease in the cycle period t_{cd} with increasing current I [Fig. S2(a) in Supplementary Materials] which was more significant than the concurrent increase in the instantaneous total heat generation rate $\dot{Q}_T(t)$ (in W) [Figs. 7(a) and 7(c)]. By contrast, Q_T increased with increasing current I for the cell with $Ti_2Nb_2O_9$ nanoparticles as the increase in $\dot{Q}_T(t)$ [Figs. 7(b) and 7(d)] was more significant than the decrease in t_{cd} [Fig. S2(b)]. Finally, for both cells at any given current I, the total dissipated thermal energy Q_T measured by *operando* isothermal calorimetry fell within 10% of the net electrical energy loss ΔE_e measured by the potentiostat. In other words, the net electrical energy loss was entirely dissipated in the form of heat. These results confirm the accuracy of our measurements.

5. Conclusion

This study investigates the tunnel-structured $Ti_2Nb_2O_9$ with fast charging capabilities at potentials above 1.0 V vs. Li/Li^+ which reduces SEI and dendrite formation. A novel sol-gel method was proposed to synthesize $Ti_2Nb_2O_9$ nanoparticles for use in lithium-ion battery electrodes. These electrodes were compared with those made of $Ti_2Nb_2O_9$ microparticles synthesized by the traditional solid-state method using unique characterization techniques including potentiometric entropy measurements and *operando* isothermal calorimetry. Cyclic voltammetry and galvanostatic cycling demonstrated the superior specific capacity, greater cycling reversibility, and smaller capacity drop with increasing current for electrodes made of $Ti_2Nb_2O_9$ nanoparticles compared to those made of $Ti_2Nb_2O_9$ microparticles. Furthermore, *in situ* XRD measurements revealed only minor and reversible distortions to the crystallographic structure of $Ti_2Nb_2O_9$. In addition, potentiometric entropy measurements indicated that both types of electrodes underwent lithium ion intercalation/deintercalation in a homogeneous solid solution of $Ti_2Nb_2O_9$ during cycling. In fact, overlapping entropic potential profiles suggested that the particle size had no influence on the thermodynamics behavior of $Ti_2Nb_2O_9$. However, electrodes made of $Ti_2Nb_2O_9$ nanoparticles exhibited smaller overpotential than those made of $Ti_2Nb_2O_9$ microparticles, thanks to their smaller particle size and larger specific surface area which facilitate lithium ion transport. This, along with their larger electrical conductivity and thus smaller resistive losses, contributed to the smaller instantaneous and time-averaged irreversible heat generation rates at electrodes made of $Ti_2Nb_2O_9$ nanoparticles than those made of $Ti_2Nb_2O_9$ microparticles at any given C-rate, as determined by *operando* isothermal calorimetry.

CRediT authorship contribution statement

Yucheng Zhou: Conceptualization, Data curation, Formal analysis, Investigation, Visualization, Writing – original draft, Writing – review & editing. **Etienne Le Calvez:** Conceptualization, Formal analysis, Investigation, Visualization, Writing – original draft, Writing – review & editing. **Sun Woong Baek:** Conceptualization, Investigation, Writing – review & editing. **Matevž Frajnkovič:** Conceptualization, Investigation, Writing – review & editing. **Camille Douard:** Investigation. **Eric Gautron:** Investigation. **Olivier Crosnier:** Conceptualization, Supervision, Writing – review & editing. **Thierry Brousse:** Conceptualization, Funding acquisition, Supervision, Writing – review & editing. **Laurent Pilon:** Conceptualization, Funding acquisition, Project administration, Supervision, Writing – review & editing.

Declaration of Competing Interest

The authors declare that they have no known competing financial interests or personal relationships that could have appeared to influence the work reported in this paper.

Acknowledgment

This work was supported in part by the Center for Synthetic Control Across Length-scales for Advancing Rechargeables (SCALAR), an Energy Frontier Research Center funded by the U.S. Department of Energy, Office of Science, Basic Energy Sciences, under Award No. DE-SC0019381. E.L.C., C.D., E.G., O.C., and T.B. would like to acknowledge Nantes Université/NExT program (ANR-16-IDEX-0007, DISCUSS project) and Labex STORE-EX (ANR-10LABX-76-01) for financial support. The authors would like to thank Barbara Daffos for performing and analyzing low-temperature nitrogen adsorption porosimetry measurements.

Supplementary material

Supplementary material associated with this article can be found, in the online version, at doi:10.1016/j.ensm.2022.08.010.

References

[1] P. Zhai, L. Liu, X. Gu, T. Wang, Y. Gong, Interface engineering for lithium metal anodes in liquid electrolyte, Adv. Energy Mater. 10 (34) (2020) 2001257, https://doi.org/10.1002/aenm.202001257.

[2] Y. Han, B. Liu, Z. Xiao, W. Zhang, X. Wang, G. Pan, Y. Xia, X. Xia, J. Tu, Interface issues of lithium metal anode for high-energy batteries: challenges, strategies, and perspectives, InfoMat 3 (2) (2021) 155–174, https://doi.org/10.1002/inf2.12166.

[3] K. Song, D.-H. Seo, M.R. Jo, Y.-I. Kim, K. Kang, Y.-M. Kang, Tailored oxygen framework of $Li_4Ti_5O_{12}$ nanorods for high-power Li ion battery, J. Phys. Chem. Lett. 5 (8) (2014) 1368–1373, https://doi.org/10.1021/jz5002924.

[4] M.M. Thackeray, K. Amine, $Li_4Ti_5O_{12}$ spinel anodes, Nat. Energy 6 (6) (2021) 683, https://doi.org/10.1038/s41560-021-00829-2.

[5] V. Augustyn, J. Come, M.A. Lowe, J.W. Kim, P.-L. Taberna, S.H. Tolbert, H. D. Abruna, P. Simon, B. Dunn, High-rate electrochemical energy storage through Li^+ intercalation pseudocapacitance, Nat. Mater. 12 (6) (2013) 518–522, https://doi.org/10.1038/nmat3601.

[6] J. Come, V. Augustyn, J.W. Kim, P. Rozier, P.-L. Taberna, P. Gogotsi, J.W. Long, B. Dunn, P. Simon, Electrochemical kinetics of nanostructured Nb_2O_5 electrodes, J. Electrochem. Soc. 161 (5) (2014) A718–A725, https://doi.org/10.1149/2.040405jes.

[7] K.J. Griffith, Y. Harada, S. Egusa, R.M. Ribas, R.S. Monteiro, R.B.V. Dreele, K. A. Cheetham, R.J. Cava, C.P. Grey, J.B. Goodenough, Titanium niobium oxide: from discovery to application in fast-charging lithium-ion batteries, Chem. Mater. 33 (1) (2021) 4–18, https://doi.org/10.1021/acs.chemmater.0c02955.

[8] K.J. Griffith, K.M. Wiaderek, G. Cibin, L.E. Marbella, C.P. Grey, Niobium tungsten oxides for high-rate lithium-ion energy storage, Nature 559 (7715) (2018) 556–563, https://doi.org/10.1038/s41586-018-0347-0.

[9] M.B. Preefer, M. Saber, Q. Wei, N.H. Bashian, J.D. Bocarsly, W. Zhang, G. Lee, J. Milam-Guerrero, E.S. Howard, R.C. Vincent, B.C. Melot, A.V. der Ven, R. Seshadri, B.S. Dunn, Multielectron redox and insulator-to-metal transition upon lithium insertion in the fast-charging, Wadsley-Roth phase PNb_9O_{25}, Chem. Mater. 32 (11) (2020) 4553–4563, https://doi.org/10.1021/acs.chemmater.0c00560.

[10] M. Saber, M.B. Preefer, S.K. Kolli, W. Zhang, G. Laurita, B. Dunn, R. Seshadri, A. V. der Ven, Role of electronic structure in Li ordering and chemical strain in the fast charging Wadsley-Roth phase PNb_9O_{25}, Chem. Mater. 33 (19) (2021) 7755–7766, https://doi.org/10.1021/acs.chemmater.1c02059.

[11] S.W. Baek, M.B. Preefer, M. Saber, K. Zhai, M. Frajnkovič, Y. Zhou, B.S. Dunn, A. V. der Ven, R. Seshadri, L. Pilon, Potentiometric entropy and *operando*calorimetric measurements reveal fast charging mechanisms in PNb_9O_{25}, J. Power Sources 520 (2022) 230776, https://doi.org/10.1016/j.jpowsour.2021.230776.

[12] J.-F. Colin, V. Pralong, M. Hervieu, V. Caignaert, B. Raveau, New titanoniobates $(Li,H)_2TiNbO_5$ and $(Li,H)_3TiNbO_5$: synthesis, structure and properties, J. Mater. Chem. 18 (26) (2008) 3121–3128, https://doi.org/10.1039/B801368C.

[13] J.-F. Colin, V. Pralong, M. Hervieu, V. Caignaert, B. Raveau, Lithium insertion in an oriented nanoporous oxide with a tunnel structure: $Ti_2Nb_2O_9$, Chem. Mater. 20 (4) (2008) 1534–1540, https://doi.org/10.1021/cm702978g.

[14] O.A. Drozhzhin, V.V. Grigoryev, A.M. Alekseeva, R.R. Samigullin, D.A. Aksyonov, O.V. Boytsova, D. Chernyshov, V.V. Shapovalov, A.A. Guda, A.V. Soldatov, K. J. Stevenson, A.M. Abakumov, E.V. Antipov, Revisited $Ti_2Nb_2O_9$ as an anode material for advanced Li-ion batteries, ACS Appl. Mater. Interfaces 13 (47) (2021) 56366–56374, https://doi.org/10.1021/acsami.1c20842.

[15] W. Du, A. Gupta, X. Zhang, A.M. Sastry, W. Shyy, Effect of cycling rate, particle size and transport properties on lithium-ion cathode performance, Int. J. Heat Mass Transf. 53 (17) (2010) 3552–3561, https://doi.org/10.1016/j.ijheatmasstransfer.2010.04.017.

[16] A.K. Rai, L.T. Anh, J. Gim, V. Mathew, J. Kang, B.J. Paul, J. Song, J. Kim, Simple synthesis and particle size effects of TiO_2 nanoparticle anodes for rechargeable lithium ion batteries, Electrochim. Acta 90 (2013) 112–118, https://doi.org/10.1016/j.electacta.2012.11.104.

[17] S.-K. Jung, I. Hwang, D. Chang, K.-Y. Park, S.J. Kim, W.M. Seong, D. Eum, J. Park, B. Kim, J. Kim, J.H. Heo, K. Kang, Nanoscale phenomena in lithium-ion batteries, Chem. Rev. 120 (14) (2020) 6684–6737, https://doi.org/10.1021/acs.chemrev.9b00405.

[18] J. Zhang, Z. Li, Q. Fu, Y. Xue, Z. Cui, The size-dependence of electrochemical thermodynamics of metal nanoparticles electrodes in theory and experiment, J. Electrochem. Soc. 164 (12) (2017) H828–H835, https://doi.org/10.1149/2.1741712jes.

[19] K. Kai, Y. Kobayashi, H. Miyashiro, G. Oyama, S. Nishimura, M. Okubo, A. Yamada, Particle-size effects on the entropy behavior of a Li_xFePO_4 electrode, Chemphyschem 15 (10) (2014) 2156–2161, https://doi.org/10.1002/cphc.201301219.

[20] K. Shen, H. Chen, F. Klaver, F.M. Mulder, M. Wagemaker, Impact of particle size on the non-equilibrium phase transition of lithium-inserted anatase TiO_2, Chem. Mater. 26 (4) (2014) 1608–1615, https://doi.org/10.1021/cm4037346.

[21] L. Shen, Y. Wang, H. Lv, S. Chen, P.A. van Aken, X. Wu, J. Maier, Y. Yu, Ultrathin $Ti_2Nb_2O_9$ nanosheets with pseudocapacitive properties as superior anode for sodium-ion batteries, Adv. Mater. 30 (51) (2018) 1804378, https://doi.org/10.1002/adma.201804378.

[22] L. She, F. Zhang, C. Jia, L. Kang, Q. Li, X. He, J. Sun, Z. Lei, Z.-H. Liu, $Ti_2Nb_2O_9$/graphene hybrid anode with superior rate capability for high-energy-density sodium-ion capacitors, J. Alloys Compd. 860 (2021) 158431, https://doi.org/10.1016/j.jallcom.2020.158431.

[23] L. She, F. Zhang, C. Jia, L. Kang, Q. Li, X. He, J. Sun, Z. Lei, Z.-H. Liu, Ultrahigh-energy sodium ion capacitors enabled by the enhanced intercalation pseudocapacitance of self-standing $ti_2nb_2o_9$/CNF anodes, Nanoscale 13 (37) (2021) 15781–15788, https://doi.org/10.1039/D1NR04241F.

[24] N. Mahmood, Y. Hou, Electrode nanostructures in lithium-based batteries, Adv. Sci. 1 (1) (2014) 1400012, https://doi.org/10.1002/advs.201400012.

[25] Y. Sun, N. Liu, Y. Cui, Promises and challenges of nanomaterials for lithium-based rechargeable batteries, Nat. Energy 1 (7) (2016) 16071, https://doi.org/10.1038/nenergy.2016.71.

[26] E. Pomerantseva, F. Bonaccorso, X. Feng, Y. Cui, Y. Gogotsi, Energy storage: the future enabled by nanomaterials, Science 366 (6468) (2019) eaan8285, https://doi.org/10.1126/science.aan8285.

[27] J. Livage, M. Henry, C. Sanchez, Sol-gel chemistry of transition metal oxides, Prog. Solid State Chem. 18 (4) (1988) 259–341, https://doi.org/10.1016/0079-6786(88)90005-2.

[28] A.V. der Ven, J. Bhattacharya, A.A. Belak, Understanding Li diffusion in Li-intercalation compounds, Acc. Chem. Res. 46 (5) (2013) 1216–1225, https://doi.org/10.1021/ar200329r.

[29] M.J. Moran, H.N. Shapiro, D.D. Boettner, M.B. Bailey, Fundamentals of Engineering Thermodynamics, John Wiley & Sons, New York, NY, 2018.

[30] S.W. Baek, K.E. Wyckoff, D.M. Butts, J. Bienz, A. Likitchatchawankun, M. B. Preefer, M. Frajnkovič, B.S. Dunn, R. Seshadri, L. Pilon, *Operando* calorimetry informs the origin of rapid rate performance in microwave-prepared $TiNb_2O_7$ electrodes, J. Power Sources 490 (2021) 229537, https://doi.org/10.1016/j.jpowsour.2021.229537.

[31] W. Weppner, R.A. Huggins, Determination of the kinetic parameters of mixed-conducting electrodes and application to the system Li_3Sb, J. Electrochem. Soc. 124 (10) (1977) 1569–1578, https://doi.org/10.1149/1.2133112.

[32] J. Newman, K.E. Thomas, H. Hafezi, D.R. Wheeler, Modeling of lithium-ion batteries, J. Power Sources 119 (2003) 838–843, https://doi.org/10.1016/S0378-7753(03)00282-9.

[33] G. Liu, M. Ouyang, L. Lu, J. Li, X. Han, Analysis of the heat generation of lithium-ion battery during charging and discharging considering different influencing factors, J. Therm. Anal. Calorim. 116 (2) (2014) 1001–1010, https://doi.org/10.1007/s10973-013-3599-9.

[34] G. Assat, S.L. Glazier, C. Delacourt, J.-M. Tarascon, Probing the thermal effects of voltage hysteresis in anionic redox-based lithium-rich cathodes using isothermal calorimetry, Nat. Energy 4 (8) (2019) 647–656, https://doi.org/10.1038/s41560-019-0410-6.

[35] K.E. Thomas, J. Newman, Thermal modeling of porous insertion electrodes, J. Electrochem. Soc. 150 (2) (2003) A176–A192, https://doi.org/10.1149/1.1531194.

[36] S. Ma, M. Jiang, P. Tao, C. Song, J. Wu, J. Wang, T. Deng, W. Shang, Temperature effect and thermal impact in lithium-ion batteries: a review, Prog. Nat. Sci. 28 (6) (2018) 653–666, https://doi.org/10.1016/j.pnsc.2018.11.002.

[37] D. Andre, M. Meiler, K. Steiner, C. Wimmer, T. Soczka-Guth, D.U. Sauer, Characterization of high-power lithium-ion batteries by electrochemical impedance spectroscopy. I. Experimental investigation, J. Power Sources 196 (12) (2011) 5334–5341, https://doi.org/10.1016/j.jpowsour.2010.12.102.

[38] M. Ecker, J.B. Gerschler, J. Vogel, S. Kabitz, F. Hust, P. Dechent, D.U. Sauer, Development of a lifetime prediction model for lithium-ion batteries based on extended accelerated aging test data, J. Power Sources 215 (2012) 248–257, https://doi.org/10.1016/j.jpowsour.2012.05.012.

[39] Y. Bai, L. Li, Y. Li, G. Chen, H. Zhao, Z. Wang, C. Wu, H. Ma, X. Wang, H. Cui, J. Zhou, Reversible and irreversible heat generation of NCA/Si-C pouch cell during electrochemical energy-storage process, J. Energy Chem. 29 (2019) 95–102, https://doi.org/10.1016/j.jechem.2018.02.016.

[40] O. Munteshari, J. Lau, D.S. Ashby, B. Dunn, L. Pilon, Effects of constituent materials on heat generation in individual EDLC electrodes, J. Electrochem. Soc. 165 (7) (2018) A1547–A1557, https://doi.org/10.1149/2.0771807jes.

[41] A. Likitchatchawankun, A. Kundu, O. Munteshari, T.S. Fisher, L. Pilon, Heat generation in all-solid-state supercapacitors with graphene electrodes and gel electrolytes, Electrochim. Acta 303 (2019) 341–353, https://doi.org/10.1016/j.electacta.2019.02.031.

[42] O. Munteshari, J. Lau, A. Likitchatchawankun, B.-A. Mei, C.S. Choi, D. Butts, B. S. Dunn, L. Pilon, Thermal signature of ion intercalation and surface redox reactions mechanisms in model pseudocapacitive electrodes, Electrochim. Acta 307 (2019) 512–524, https://doi.org/10.1016/j.electacta.2019.03.185.

[43] A. Likitchatchawankun, G. Whang, J. Lau, O. Munteshari, B. Dunn, L. Pilon, Effect of temperature on irreversible and reversible heat generation rates in ionic liquid-based electric double layer capacitors, Electrochim. Acta 338 (2020) 135802, https://doi.org/10.1016/j.electacta.2020.135802.

[44] O. Munteshari, A. Borenstein, R.H. DeBlock, J. Lau, G. Whang, Y. Zhou, A. Likitchatchawankun, R.B. Kaner, B. Dunn, L. Pilon, *In operando* calorimetric measurements for activated carbon electrodes in ionic liquid electrolytes under

large potential windows, ChemSusChem 13 (5) (2020) 1013–1026, https://doi.org/10.1002/cssc.201903011.

[45] A. Likitchatchawankun, R.H. DeBlock, G. Whang, O. Munteshari, M. Frajnkovič, B. S. Dunn, L. Pilon, Heat generation in electric double layer capacitors with neat and diluted ionic liquid electrolytes under large potential window between 5 and 80 °C, J. Power Sources 488 (2021) 229368, https://doi.org/10.26434/chemrxiv.13168349.

[46] D.M. Seo, S. Reininger, M. Kutcher, K. Redmond, W.B. Euler, B.L. Lucht, Role of mixed solvation and ion pairing in the solution structure of lithium ion battery electrolytes, J. Phys. Chem. C 119 (25) (2015) 14038–14046, https://doi.org/10.1021/acs.jpcc.5b03694.

[47] O. Borodin, M. Olguin, P. Ganesh, P.R.C. Kent, J.L. Allen, W.A. Henderson, Competitive lithium solvation of linear and cyclic carbonates from quantum chemistry, PCCP 18 (1) (2016) 164–175, https://doi.org/10.1039/C5CP05121E.

[48] W. Cui, Y. Lansac, H. Lee, S.-T. Hong, Y.H. Jang, Lithium ion solvation by ethylene carbonates in lithium-ion battery electrolytes, revisited by density functional theory with the hybrid solvation model and free energy correction in solution, PCCP 18 (34) (2016) 23607–23612, https://doi.org/10.1039/C6CP01667G.

[49] M. Shakourian-Fard, G. Kamath, S.K.R.S. Subramanian , Evaluating the free energies of solvation and electronic structures of lithium-ion battery electrolytes, Chemphyschem 17 (18) (2016) 2916–2930, https://doi.org/10.1002/cphc.201600338.

[50] C.L. Berhaut, D. Lemordant, P. Porion, L. Timperman, G. Schmidt, M. Anouti, Ionic association analysis of LiTDI, LiFSI and $LiPF_6$ in EC/DMC for better Li-ion battery performances, RSC Adv. 9 (8) (2019) 4599–4608, https://doi.org/10.1039/C8RA08430K.

[51] W. Lu, J. Prakash, *In situ* measurements of heat generation in a Li/mesocarbon microbead half-cell, J. Electrochem. Soc. 150 (3) (2003) A262–A266, https://doi.org/10.1149/1.1541672.

[52] K.E. Thomas, J. Newman, Heats of mixing and of entropy in porous insertion electrodes, J. Power Sources 119 (2003) 844–849, https://doi.org/10.1016/S0378-7753(03)00283-0.

[53] K. Smith, C.-Y. Wang, Power and thermal characterization of a lithium-ion battery pack for hybrid-electric vehicles, J. Power Sources 160 (1) (2006) 662–673, https://doi.org/10.1016/j.jpowsour.2006.01.038.

[54] A.V. der Ven, K.A. See, L. Pilon, Hysteresis in electrochemical systems, Battery Energy 1 (2) (2022) 20210017, https://doi.org/10.1002/bte2.20210017.

[55] A.D. Wadsley, Alkali titanoniobates: the crystal structures of $KTiNbO_5$ and KTi_3NbO_9, Acta Crystallogr. 17 (6) (1964) 623–628, https://doi.org/10.1107/S0365110X64001530.

[56] M. Fang, C.H. Kim, T.E. Mallouk, Dielectric properties of the lamellar niobates and titanoniobates $AM_2Nb_3O_{10}$ and $ATiNbO_5$ (A = H, K, M = Ca, Pb), and their condensation products $Ca_4Nb_6O_{19}$ and $Ti_2Nb_2O_9$, Chem. Mater. 11 (6) (1999) 1519–1525, https://doi.org/10.1021/cm981065s.

[57] Y. Gogotsi, P. Simon, True performance metrics in electrochemical energy storage, Science 334 (6058) (2011) 917–918, https://doi.org/10.1126/science.1213003.

[58] J.B. Leriche, S. Hamelet, J. Shu, M. Morcrette, C. Masquelier, G. Ouvrard, M. Zerrouki, P. Soudan, S. Belin, E. Elkaim, F. Baudelet, An electrochemical cell for *operando* study of lithium batteries using synchrotron radiation, J. Electrochem. Soc. 157 (5) (2010) A606–A610, https://doi.org/10.1149/1.3355977.

[59] H. Wang, L. Pilon, Reply to comments on "Intrinsic limitations of impedance measurements in determining electric double layer capacitances" by H. Wang, L. Pilon [Electrochimica Acta 63 (2012) 55], Electrochim. Acta 76 (2012) 529–531, https://doi.org/10.1016/j.electacta.2012.05.039.

[60] A. Burke, M. Miller, Testing of electrochemical capacitors: capacitance, resistance, energy density, and power capability, Electrochim. Acta 55 (25) (2010) 7538–7548, https://doi.org/10.1016/j.electacta.2010.04.074.

[61] M.D. Stoller, R.S. Ruoff, Best practice methods for determining an electrode material's performance for ultracapacitors, Energy Environ. Sci. 3 (9) (2010) 1294–1301, https://doi.org/10.1039/c0ee00074d.

[62] S. Zhao, F. Wu, L. Yang, L. Gao, A.F. Burke, A measurement method for determination of dc internal resistance of batteries and supercapacitors, Electrochem. Commun. 12 (2) (2010) 242–245, https://doi.org/10.1016/j.elecom.2009.12.004.

[63] B.-A. Mei, O. Munteshari, J. Lau, B. Dunn, L. Pilon, Physical interpretations of Nyquist plots for EDLC electrodes and devices, J. Phys. Chem. C 122 (1) (2018) 194–206, https://doi.org/10.1021/acs.jpcc.7b10582.

[64] O. Munteshari, J. Lau, A. Krishnan, B. Dunn, L. Pilon, Isothermal calorimeter for measurements of time-dependent heat generation rate in individual supercapacitor electrodes, J. Power Sources 374 (2018) 257–268, https://doi.org/10.1016/j.jpowsour.2017.11.012.

[65] M. Thommes, K. Kaneko, A.V. Neimark, J.P. Olivier, F. Rodriguez-Reinoso, J. Rouquerol, K.S.W. Sing, Physisorption of gases, with special reference to the evaluation of surface area and pore size distribution (IUPAC Technical Report), Pure Appl. Chem. 87 (9–10) (2015) 1051–1069, https://doi.org/10.1515/pac-2014-1117.

[66] H. Rebbah, G. Desgardin, B. Raveau, Les oxydes $ATiMO_5$: echangeurs cationiques, Mater. Res. Bull. 14 (9) (1979) 1125–1131, https://doi.org/10.1016/0025-5408(79)90206-X.

[67] J. Huang, Z. Wang, M. Hou, X. Dong, Y. Liu, Y. Wang, Y. Xia, Polyaniline-intercalated manganese dioxide nanolayers as a high-performance cathode material for an aqueous zinc-ion battery, Nat. Commun. 9 (1) (2018) 2906, https://doi.org/10.1038/s41467-018-04949-4.

[68] R.J. Cava, D.W. Murphy, S.M. Zahurak, Lithium insertion in Wadsley-Roth phases based on niobium oxide, J. Electrochem. Soc. 130 (12) (1983) 2345–2351, https://doi.org/10.1149/1.2119583.

[69] S. Patoux, M. Dolle, G. Rousse, C. Masquelier, A reversible lithium intercalation process in an ReO_3 type structure PNb_9O_{25}, J. Electrochem. Soc. 149 (4) (2002) A391–A400, https://doi.org/10.1149/1.1455647.

[70] J. Wang, J. Polleux, J. Lim, B. Dunn, Pseudocapacitive contributions to electrochemical energy storage in TiO_2 (anatase) nanoparticles, J. Phys. Chem. C 111 (40) (2007) 14925–14931, https://doi.org/10.1021/jp074464w.

[71] H.-L. Girard, H. Wang, A. d'Entremont, L. Pilon, Physical interpretation of cyclic voltammetry for hybrid pseudocapacitors, J. Phys. Chem. C 119 (21) (2015) 11349–11361, https://doi.org/10.1021/acs.jpcc.5b00641.

[72] H.-L. Girard, B. Dunn, L. Pilon, Simulations and interpretation of three-electrode cyclic voltammograms of pseudocapacitive electrodes, Electrochim. Acta 211 (2016) 420–429, https://doi.org/10.1016/j.electacta.2016.06.066.

[73] A. Tornheim, D.C. O`Hanlon, What do coulombic efficiency and capacity retention truly measure? A deep dive into cyclable lithium inventory, limitation type, and redox side reactions, J. Electrochem. Soc. 167 (11) (2020) 110520, https://doi.org/10.1149/1945-7111/ab9ee8.

[74] J. Shim, K.A. Striebel, Effect of electrode density on cycle performance and irreversible capacity loss for natural graphite anode in lithium-ion batteries, J. Power Sources 119–121 (2003) 934–937, https://doi.org/10.1016/S0378-7753(03)00235-0.

[75] H. Buqa, D. Goers, M. Holzapfel, M.E. Spahr, P. Novak, High rate capability of graphite negative electrodes for lithium-ion batteries, J. Electrochem. Soc. 152 (2) (2005) A474–A481, https://doi.org/10.1149/1.1851055.

[76] X. Li, P. Yan, X. Xiao, J.H. Woo, C. Wang, J. Liu, J.-G. Zhang, Design of porous Si/C-graphite electrodes with long cycle stability and controlled swelling, Energy Environ. Sci. 10 (6) (2017) 1427–1434, https://doi.org/10.1039/C7EE00838D.

[77] D. Rehnlund, Z. Wang, L. Nyholm, Lithium-diffusion induced capacity losses in lithium-based batteries, Adv. Mater. 34 (19) (2022) 2108827, https://doi.org/10.1002/adma.202108827.

[78] N.S. Hudak, L.E. Davis, G. Nagasubramanian, Cycling-induced changes in the entropy profiles of lithium cobalt oxide electrodes, J. Electrochem. Soc. 162 (3) (2015) A315–A321, https://doi.org/10.1149/2.0071503jes.

[79] H. Liu, M. Wolfman, K. Karki, Y.-S. Yu, E.A. Stach, J. Cabana, K.W. Chapman, P. J. Chupas, Intergranular cracking as a major cause of long-term capacity fading of layered cathodes, Nano Lett. 17 (6) (2017) 3452–3457, https://doi.org/10.1021/acs.nanolett.7b00379.

[80] P. Yan, J. Zheng, M. Gu, J. Xiao, J.-G. Zhang, C.-M. Wang, Intragranular cracking as a critical barrier for high-voltage usage of layer-structured cathode for lithium-ion batteries, Nat. Commun. 8 (1) (2017) 14101, https://doi.org/10.1038/ncomms14101.

[81] A.J. Merryweather, Q. Jacquet, S.P. Emge, C. Schnedermann, A. Rao, C.P. Grey, *Operando* monitoring of single-particle kinetic state-of-charge heterogeneities and cracking in high-rate li-ion anodes, arXiv (2021), https://doi.org/10.48550/arXiv.2111.11997.

[82] F. Hao, A. Verma, P.P. Mukherjee, Mechanistic insight into dendrite-SEI interactions for lithium metal electrodes, J. Mater. Chem. A 6 (40) (2018) 19664–19671, https://doi.org/10.1039/C8TA07997H.

[83] U. Janakiraman, T.R. Garrick, M.E. Fortier, Review–lithium plating detection methods in Li-ion batteries, J. Electrochem. Soc. 167 (16) (2020) 160552, https://doi.org/10.1149/1945-7111/abd3b8.